This is a preprint, the final version is subject to change, of the American Mineralogist (MSA)
Cite as Authors (Year) Title. American Mineralogist, in press.
DOI: https://doi.org/10.2138/am-2018-6226

You are currently on revision 2.

Formation of dolomite catalyzed by sulfate-driven anaerobic oxidation of methane: Mineralogical and geochemical evidence from the northern South China Sea

Yang Lu[1,2,3], Xiaoming Sun[1,3,4,*], Huifang Xu[2,*], Hiromi Konishi[2,†], Zhiyong Lin[4], Li Xu[1,3], Tingting Chen[1,3], Xinrong Hao[4], Hongfeng Lu[5], Jörn Peckmann[6]

[1]School of Marine Sciences, Sun Yat-sen University, Guangzhou 510006, China

[2]NASA Astrobiology Institute, Department of Geoscience, University of Wisconsin-Madison, Madison, WI 53706

[3]Guangdong Provincial Key Laboratory of Marine Resources and Coastal Engineering, Guangzhou 510275, China

[4]School of Earth Science and Engineering, Sun Yat-sen University, Guangzhou 510275, China

[5]Guangzhou Marine Geological Survey, Guangzhou 510760, China

[6]Institute für Geologie, Universität Hamburg, 20146 Hamburg, Germany

[†]Present address: Department of Geology, Niigata University, 8050 Ikarashi 2-no-cho, Nishi-ku, 12 Niigata 950-2181, Japan

*Corresponding authors:

Prof. Xiaoming Sun, tel: 86-20-84110968, E-mail: eessxm@mail.sysu.edu.cn

Prof. Huifang Xu, tel: 1-608-265-5887, E-mail: hfxu@geology.wisc.edu

E-mails:

Yang Lu: luyang26@mail.sysu.edu.cn

Hiromi Konishi: hkonishi@geo.sc.niigata-u.ac.jp

Zhiyong Lin: linzhiy3@mail2.sysu.edu.cn

Li Xu: xu-bluesky@126.com

Tingting Chen: 1940163425@qq.com

Xinrong Hao: haoxr@mail.sysu.edu.cn

Hongfeng Lu: gmgslhf@126.com

Jörn Peckmann: joern.peckmann@uni-hamburg.de

This is a preprint, the final version is subject to change, of the American Mineralogist (MSA)
Cite as Authors (Year) Title. American Mineralogist, in press.
DOI: https://doi.org/10.2138/am-2018-6226

ABSTRACT

It is very difficult to synthesize dolomite under Earth-surface conditions in the laboratory. However, multiple carbonate phases, including low-Mg-calcite (LMC), high-Mg-calcite (HMC), and dolomite, have been discovered in authigenic carbonate deposits that precipitated at cold methane seeps. The formation of such seep carbonates is triggered by the sulfate-driven anaerobic oxidation of methane (SD-AOM), which is mediated by a consortium of methane-oxidizing archaea and sulfate-reducing bacteria; this process releases bicarbonate and dissolved sulfide. Thus, the formation of Ca-Mg carbonate phases and, particularly, their respective $MgCO_3$ contents are likely to be intimately related to SD-AOM and the methane supply at cold seeps. Yet, the driving forces for $MgCO_3$ enrichment and the actual mechanism responsible for the incorporation of Mg^{2+} into the crystal lattice are not fully understood. Interestingly, recent laboratory experiments succeeded in synthesizing disordered dolomite under the catalysis of dissolved sulfide and extracellular polymeric substances (EPS) at low-temperatures. To characterize the effect of these catalyses on the formation of seep carbonates, we investigated mineral phases, microstructure, and contents of Ca, Mg, and rare earth elements of seep carbonates from the Shenhu area and the Southwest (SW) Taiwan basin of the northern South China Sea (SCS). The studied carbonates are composed of multiple Ca-Mg carbonate phases, including HMC, weakly ordered dolomite, and dolomite with a wide range of $MgCO_3$ contents. Transmission electron microscopy indicates that the

57 microstructure of some Shenhu dolomite is almost stoichiometric, only a few domains
58 exhibit the structure of Mg-calcite. Weakly ordered dolomite from the SW Taiwan basin
59 contains less $MgCO_3$ than the Shenhu dolomite, and is composed of heterogeneously
60 distributed domains of Mg-calcite and dolomite. A positive correlation between $MgCO_3$
61 contents, cerium anomalies, Nd_N to Yb_N ratios, and ^{13}C-depletion suggests that Mg^{2+}
62 incorporation into the crystal lattice is favored by reducing conditions produced by
63 pronounced SD-AOM. Based on previous studies, we put forward that SD-AOM derived
64 sulfide and EPS produced by the SD-AOM consortium are the most plausible drivers for
65 Ca-Mg carbonate formation at cold seeps. Precipitated under conditions similar to
66 laboratory experiments, the initial Ca-Mg carbonates are apparently disordered
67 nano-crystals with various $MgCO_3$ contents. In the course of maturation and
68 recrystallization, the Ca-Mg carbonates evolve into weakly ordered dolomite or dolomite.
69 This study contributes to the understanding of dolomite formation at cold seeps and the
70 relationship between carbonate mineralogy, the supply of methane, and microbial
71 activity.

72 **Keywords:** Dolomite, dolomite problem, authigenic Ca-Mg carbonate, SD-AOM, cold
73 seep, South China Sea

74

75

76

This is a preprint, the final version is subject to change, of the American Mineralogist (MSA)
Cite as Authors (Year) Title. American Mineralogist, in press.
DOI: https://doi.org/10.2138/am-2018-6226

77

78 ## INTRODUCTION

79 The problem of sedimentary dolomite formation has sustained for over 200 years
80 (Lippmann, 1973; Hardie, 1987; Burns et al., 2000; Warren, 2000; Machel, 2004). The
81 dolomite content of sedimentary rock that formed before the Pleistocene is much higher
82 than that of modern sediments and laboratory syntheses of ordered and stoichiometric
83 dolomite at surface conditions have not succeeded (Lippmann, 1973; Land, 1998; Burns
84 et al., 2000; Machel, 2004; Gregg et al., 2015). Several models of dolomite formation
85 have been suggested based on studies of different geological settings (Zenger and
86 Dunham, 1980; Hardie, 1987; Warren, 2000; Machel, 2004), but primary or
87 penecontemporaneous dolomite formation as opposed to dolomitization is still
88 insufficiently understood. Sulfate was once considered as a major factor that inhibits
89 primary dolomite formation (Baker and Kastner, 1981; Compton, 1988). However, an
90 inhibition effect prevails when the concentration of sulfate in the fluid from which
91 carbonate minerals precipitate is low, which is not the case under conditions of dolomite
92 precipitation in marine environments (Hardie, 1987; Brady et al., 1996; Machel, 2004). It
93 seems likely that one of the rate-limiting steps of dolomite precipitation is the
94 dehydration of Mg^{2+} ions. As the dehydration of Ca^{2+} ions is much easier than that of
95 Mg^{2+} ions, more Ca^{2+} than Mg^{2+} enters the cation sites of initially formed layers of
96 Ca-Mg carbonate minerals (Pokrovsky, 1998; Higgins and Hu, 2005; Hu et al., 2005;

97 Romanek et al., 2009). The few incorporated Mg^{2+} ions distort the lattice structure
98 (Wasylenki et al., 2005; Xu et al., 2013), making the new layer unstable and preventing
99 the growth of Ca-Mg carbonates (Mazzullo, 2000; de Leeuw and Parker, 2001; Fenter et
100 al., 2007). For dolomite to form under surface conditions, the kinetic barrier to
101 Mg^{2+}-water dehydration must be overcome (Lippmann, 1973; Brady, et al., 1996; Land,
102 1998; de Leeuw, 2002; Machel, 2004). Some studies suggested that microorganisms can
103 assist in dolomite formation by creating Mg^{2+}- and bicarbonate-rich and sulfate-free
104 conditions in micro-environments affected by sulfate reduction (Vasconcelos and
105 McKenzie, 1997; Wright, 1999; Van Lith, et al., 2003a) or by providing extracellular
106 polymeric substances (EPS) as nucleation sites for dolomite precipitation (Riding, 2000;
107 Van Lith, et al., 2003b; Roberts et al., 2004; Ayllón-Quevedo, et al., 2007; Perri and
108 Tucker, 2007). Dead cell pellets of some anaerobic microorganisms have been found to
109 be unable to promote the formation of dolomite after EPS extraction (Zhang et al., 2015),
110 whereas microbially produced carbonate ions, dissolved sulfide, and EPS are able to
111 facilitate the dehydration of Mg^{2+} and the precipitation of Ca-Mg carbonates including
112 disordered dolomite (Lippmann, 1973; Zhang et al., 2012a, 2012b, 2015). However,
113 recent studies indicate that Mg^{2+} dehydration alone is not sufficient to form ordered
114 dolomite. On the one hand, synthesis of Ca-Mg carbonates in anhydrous solvent with
115 Mg/Ca ratios of seawater resulted in amorphous phases, although with high $MgCO_3$
116 contents (Xu et al., 2013). On the other hand, the incorporation of Ba^{2+} and Mg^{2+} at

similar rates into norsethite with dolomite-like structure put into question the inhibiting effect of a dehydration barrier of Mg^{2+} on the formation of ordered dolomite (Pimentel and Pina, 2014). A fundamental barrier has been suggested to be the factor that prevents cation ordering in Ca-Mg carbonates, which is likely to be caused by cation sizes (Xu et al., 2013; Pimentel and Pina, 2014). Perhaps, fluctuation of the conditions during precipitation, such as pH, and/or a sequence of solvent-mediated processes may facilitate formation of ordered dolomite (Liebermann, 1967; Deelman, 2011) or dolomite-like phases (Pimentel and Pina, 2014). Therefore, overcoming the intrinsic crystallographic barrier to develop cation ordering in Ca-Mg carbonates is another rate-limiting step to form ordered dolomite.

Multiple Ca-Mg carbonate phases, including LMC, HMC, and dolomite have been identified as constituents of seep deposits (Greinert et al., 2001; Roberts et al., 2010). The $MgCO_3$ content of HMC and dolomite varies over a wide range (Ferrell and Aharon, 1994; Han et al., 2008; Robert et al., 2010; Lu et al., 2015). In cold seep environments, sulfate-driven anaerobic oxidation of methane (SD-AOM), mediated by a consortium of methane-oxidizing archaea and sulfate-reducing bacteria, produces bicarbonate and sulfide and drives carbonate formation (Boetius, et al., 2000; Peckmann and Thiel, 2004; Suess, 2010, 2014).

$$CH_4 + SO_4^{2-} \rightarrow HS^- + HCO_3^- + H_2O$$

136 The released bicarbonate and sulfide trigger the precipitation of authigenic carbonates
137 and pyrite in or near the SD-AOM zone (e.g. Greinert et al., 2001; Suess, 2014; Lin et al.,
138 2016, 2017a, 2017b). Since fluid flow at seeps varies with time (e.g. Solomon et al.,
139 2008), the redox conditions during the precipitation of seep carbonates typically vary and
140 are influenced by different degrees of seawater influence on the composition of pore
141 waters, which is reflected in changing carbonate mineralogies and the patterns of
142 biomarkers, stable oxygen and sulfur isotopes of carbonate associated sulfate, magnesium
143 isotopes, and redox sensitive elements (Feng et al., 2009b, 2016; Peckmann et al., 2009;
144 Himmler et al., 2010; Birgel et al., 2011; Hu et al., 2014; Lu et al., 2017).

145 The precipitation of dolomite is believed to be facilitated by sulfate-free conditions in
146 or near the SD-AOM zone deeper in the sediment (Haas et al., 2010; Magalhães et al.,
147 2012) or by the microorganisms of the SD-AOM consortium (Han et al., 2008; Feng and
148 Roberts, 2010). However, sulfate is in fact not an effective inhibitor for dolomite
149 precipitation (Hardie, 1987; Brady et al., 1996; Machel, 2004) and dissolved sulfate does
150 not inhibit dolomite crystallization in the presence of dissolved sulfide (Zhang et al., 2012,
151 2013). Modeling, using the density functional theory, demonstrated that sulfide adsorbed
152 on dolomite surface can weaken the bond between water and surface Mg^{2+} ions (Shen et
153 al. 2014). Interestingly, SD-AOM releases sulfide ions and the SD-AOM consortium
154 produces EPS, and both dissolved sulfide and EPS have been found to be able to catalyze
155 the precipitation of dolomite. In this paper, we assess the significance of sulfide

156 production by SD-AOM for dolomite formation at seeps based on carbonate phases,
157 microstructures, carbon and oxygen isotope compositions, and rare earth element patterns
158 of authigenic carbonates from the northern South China Sea.
159

160 **SAMPLES**

161 During cruises in 2003 and 2004, two dredge surveys were carried out in the SW
162 Taiwan basin and the Shenhu area, respectively, by the research vessel "Hai Yang Si
163 Hao" of the Guangzhou Marine Geological Survey. Authigenic carbonates were sampled
164 at sites HS4 and HS4a in the Shenhu area and at the site HD314 in the SW Taiwan basin
165 (Fig. 1). The water depths of these sites were about 350 m to 400 m, respectively.
166 Favorable conditions for seep activity have been encountered in both areas. Hydrocarbon
167 source rocks are represented by Cenozoic strata (Pang et al., 2006; Huang et al., 2008;
168 Chen et al., 2009; Gong et al., 2009), which are connected with the shallow sediments by
169 tectonic pathways, such as gas chimneys, mud diapirs, mud volcanos, and normal faults
170 (Huang et al., 2008; Chen et al., 2009; Sun et al., 2012a; Sun et al., 2012b). Methane
171 enrichment was detected in the sediments of these two areas (Zhu et al., 2003; Huang et
172 al., 2006; Wu et al., 2006; Yin et al., 2008). Subsequently, a currently active cold seep
173 site was discovered by the deep submergence vehicle Jiaolong in the SW Taiwan basin
174 (Feng and Chen, 2015).

175 The surfaces of the samples from Shenhu area are smooth and dark. Polished slabs
176 reveal that the colors of rock pieces evolve from gray to brown from the near center to the
177 rim, indicating alteration after exposure to oxic seawater (Fig. 2a to e). The sample from
178 site HD314 appears yellow and porous on the surface. The internal part is mostly gray,
179 disseminated with some yellow components (Fig. 2f).
180

181 ## METHODS

182 **Powder X-ray diffraction (PXRD), scanning transmission electron microscopy**
183 **(STEM), and transmission electron microscopy (TEM) analyses**

184 Small particles of the internal unaltered parts of each sample were cut off and ground
185 into powder. About 1 mg of each sample was used for PXRD analysis. Powder was
186 loaded into a fiberglass mount and analyzed by a Rigaku Rapid II X-ray diffraction
187 system (Mo Kα radiation) in the Department of Geoscience of the University of
188 Wisconsin (UW)-Madison. The diffraction data were recorded on a plate detector and,
189 then, transformed into 2θ-intensity profiles by Rigaku's 2DP software. The d values of
190 each profile were calibrated using the profile of Si powder of SRM 610b. Major mineral
191 phases were identified with the Jade 9 software. Mineral contents were calculated using
192 the Rietveld Method, in which a simulated pattern was calculated based on each
193 identified phase to fit the experimental result. At peak overlap position, all the peaks from
194 each phase were summed up (Rietveld, 1967).

195 Small parts of the gray, internal unweathered portions of samples 4-3, 4a-2, and 314-1
196 were cut off using a diamond saw and milled to about 30 μm thick slices, with each side
197 polished. The thin slices were pasted on copper grids and ion milled by a Fischione 1010.
198 TEM-energy-dispersive X-ray spectroscopy (EDS), STEM, and selected-area electron
199 diffraction (SAED) were carried out with a FEG-(S)TEM (Titan 80-200) equipped with a
200 spherical aberration corrector in Materials Science Center of UW-Madison.
201
202 **Ca, Mg, and rare earth element (REE) contents, and C and O isotope compositions**
203 Samples for geochemical analyses were micro-drilled from polished surfaces of the
204 unweathered internal portions of samples and ground into powder. About 7 mg of each
205 sample was prepared for Ca and Mg measurements. Powder was leached by 10 ml 5
206 vol% purified acetic acid for 1 h on an oscillator to separate carbonates and residue
207 phases. After centrifugation at 4000 r/min for 10 min, the upper half solutions were
208 transferred and filtered by a Millex®GP 0.22 μm filter-unit. The cleaned solutions were
209 dried on a hotplate at 120°C. Finally, the leachates were dissolved in 3 vol% purified
210 HNO_3 and sent to Instrumental Analysis & Research Center (IARC) of Sun Yat-sen
211 University (SYSU) for ICP-AES analyses.
212 40 mg of sample was used for REE measurements. The rock powder was reacted with
213 40 ml 5 vol% purified acetic acid for 1 h on an oscillator. Afterward, the procedure was
214 similar to that for Ca and Mg measurements. After the filtered solutions were dried out,

the residues were dissolved by 2 vol% purified HNO_3 and sent to IARC of SYSU for ICP-MS analysis. The Ce/Ce^* and Pr/Pr^* denote $2Ce_N/(La+Pr)_N$ and $2Pr_N/(Ce+Nd)_N$, respectively, where N refers to normalization by the standard Post Archean Australian Shale (PAAS; McLennan, 1989).

Less than 1 mg of rock powder of each sample was transferred to a sealed vessel and heated to 70°C. The vessels were squirted with pure helium gas (99.99%) to flush out any air. Three droplets of 100% phosphate acid were injected into the vessel to turn the carbonates into carbon dioxide, which was used to obtain the stable C and O isotope compositions with a Thermo Gasbench II linked to a Delta V Advantage mass spectrometer in the School of Earth Science and Geological Engineering of SYSU. The isotopic ratios are expressed as the δ-notation (‰) relative to the V-PDB standard. The accuracy was better than ±0.1‰.

RESULTS

Carbonate mineralogy

Thin sections and STEM observation. Rock samples from both sampling areas are similar. Coarse silicate grains, such as quartz and feldspar, are cemented by a matrix of finely crystalline carbonate minerals, which are gray to brown. Bioclasts and pyrite are scattered in the carbonate matrix (Fig. 3a and 3b). Pyrite commonly fills in chambers of the tests of foraminifers; it is oxidized to different degrees (Fig. 3c), except in sample

4a-2, where pyrite is not affected by weathering. In addition to its occurrence in foraminifer tests, individual crystals of pyrite are scattered in the carbonate matrix (Fig. 3d). High-angle angular dark-field (HAADF) STEM images reveal that the interspace between carbonate crystals, about 1 μm in size, is filled by clay minerals (Fig. 4). The carbonate crystals of the samples from the Shenhu area are sub-euhedral to anhedral (Fig. 4a and 4b), while those from the SW Taiwan basin are anhedral (Fig. 4c and 4d).

PXRD results. Quartz, albite, orthoclase, illite, HMC, and dolomite are identified from the PXRD patterns (Fig. 5 and Table 1). Although the superstructure reflections or ordering reflections of dolomite, (01.–1*{note to typesetting, the minus sign is the overbar on top of the 1}*) and (01.5), are respectively overlapped by the (–201*{note to typesetting, the minus sign is the overbar on top of the 2}*) of albite and the (131) of illite (Fig. 5), superstructure reflections are shown in the electron diffraction patterns of Ca-Mg carbonates with high $MgCO_3$ content (see next paragraph). Patterns of the samples from the two sampling areas can be distinguished by the shape and the position of the (10.4) peaks of carbonate minerals, which are distributed between those of Mg-free calcite and stoichiometric dolomite (Fig. 5). Shenhu area samples are characterized by a pronounced peak close to that of stoichiometric dolomite accompanied by a wide shoulder, whereas two peaks, in between those of Mg-free calcite and dolomite, are apparent in the SW Taiwan sample 314-1. According to the classification of Lu et al. (2015), the carbonate phases of Shenhu samples are mainly dolomite with some HMC, while those of SW

Taiwan samples are HMC and dolomite. The positions of (10.4) peaks are variable among the samples, and the (10.4) peaks are broad compared with the ideal peaks of Mg-free calcite and dolomite. The results of Rietveld analysis show that the carbonate content is approximately 50 weight% to 66 weight%. In most Shenhu samples, the content of dolomite is over 50 weight% (Table 1). HMC and dolomite are unevenly distributed in the SW Taiwan sample. Some parts are dominated by HMC or dolomite, while some other parts are composed of both minerals with the content close to 30 weight%, respectively (Table 1).

TEM studies. According to PXRD results, samples 4a-2, 4-3, and 314-1 containing near-stoichiometric dolomite, Ca-rich dolomite, and HMC were selected for TEM studies. The EDS profiles show that the difference of the peak heights of Mg and Ca is increased from samples 4a-2 over 4-3 to 314-1, corresponding to a trend to lower $MgCO_3$ contents (Fig. 6). The [010]-zone axis SAED results reveal a corresponding trend. Patterns of sample 4a-2 and one carbonate mineral of sample 4-3 show bright reflections similar to those of ordered and stoichiometric dolomite (Fig. 6a and 6b) and another carbonate mineral of sample 4-3 reveals slightly weaker superstructure reflections (e.g. (00.3), see Fig. A1 for details) (Fig. 6c). Since the $MgCO_3$ contents of these minerals are similar, the SAED patterns indicate that they represent dolomite and slightly disordered dolomite. The carbonate mineral of sample 314-1 contains slightly less $MgCO_3$ but reveals much weaker intensities of the superstructure reflections (Fig. 6d), indicating that this mineral

is weakly ordered dolomite. Microstructure features are revealed by the [010]-zone axis fast Fourier transform (FFT) patterns of High-resolution TEM (HRTEM) images. Dolomite reflection patterns are displayed in most parts of the selected minerals of samples 4a-2 and 4-3. Only a few areas reveal weak superstructure reflections (Fig. 7a to 7e). In contrast, FFT patterns of calcite and dolomite structures are detected in the analyzed minerals in sample 314-1, which form three combinations in different nano-scale domains. Firstly, areas with calcite and dolomite reflection patterns are almost equal (Fig. 7f to 7j). Secondly and thirdly, the dolomite micro-areas are surrounded by calcite areas (Fig. 7k to 7o) and vice versa (Fig. 7p to 7t). Additional reflections are found in some small domains with dark contrast in HRTEM images of the three selected carbonate minerals, occurring almost midway between (00.0) and (10.4) reflections and between (00.0) and (10.–2*{note to typesetting, the minus sign is the overbar on top of the 2}*) reflections in dolomite patterns (Fig. 8a to 8f) and between (00.0) and (10.4) reflections in calcite patterns (Fig. 8g and 8h).

Carbonate geochemistry

Ca and Mg contents. The contents of Ca and Mg and Ca/Mg mole ratios of carbonate phases are shown in Table 2. The Ca content of Shenhu samples is lower than that of the SW Taiwan sample, ranging from 12.7% to 15.5% and 16.3% to 19%, respectively. Reversely, the Mg content of Shenhu samples, varying from 3.9% to 5.6%, is higher than

that of the SW Taiwan sample, which spans from 2.9% to 4.2%. The Mg/Ca mole ratios of Shenhu samples range from 0.5 to 0.67 and are overall higher than those of the SW Taiwan sample, ranging from 0.28 to 0.37.

Rare earth elements contents. The REE contents are listed in Table 3. The ΣREE of Shenhu samples range from 20 to 23 ppm and are higher than those of SW Taiwan samples, which range from 16 to 22 ppm. The cerium anomalies (Ce/Ce^*) of Shenhu samples cluster around 1.14, while those of the SW Taiwan sample cluster around 1.04. The Nd_N/Yb_N ratios, representing the enrichment of light REE (LREE) over heavy REE (HREE), increase from about 1.13 to 1.37 from the SW Taiwan sample to Shenhu samples. The PAAS-normalized patterns of all the samples show a middle REE (MREE) bulge (Fig. 9), very different from the REE pattern of seawater (Fig. A2). The Shenhu samples reveal positive Ce anomalies (Fig. 10).

C and O stable isotope compositions. The $\delta^{13}C$ values of all the samples are extremely negative (Table 2). From the SW Taiwan sample to the Shenhu samples, $\delta^{13}C$ values decrease from approximately −34 to −44‰; with $\delta^{13}C$ values decreasing, Mg/Ca ratios increase. The $\delta^{18}O$ values of Shenhu samples range from 2.5 to 3.5‰, while those of SW Taiwan samples are round 1.4‰.

DISCUSSION

Interpretation of carbonate mineralogies

315 The Mg/Ca ratios of carbonate phases from the two study areas reveal characteristic
316 differences, which are reflected in distinct carbonate mineralogies as indicated by PXRD
317 and SAED patterns as well as HRTEM images. The (10.4) peak is the most characteristic
318 feature of the PXRD patterns of Ca-Mg carbonates. This peak is broad in the SCS seep
319 carbonates, compared with the (10.4) peaks of Mg-free calcite and stoichiometric
320 dolomite (Fig. 5). Since the $d_{10.4}$ values and the 2θ of the (10.4) peak between calcite and
321 dolomite of Ca-Mg carbonates correspond to the $MgCO_3$ content (Goldsmith and Graf,
322 1958; Zhang et al., 2010) and the analyzed carbonates are well crystalized, the
323 broadening of (10.4) peaks indicate the presence of composite, shifting peaks, in accord
324 with carbonate phases with variable $MgCO_3$ contents. For example, the broadening HMC
325 peak of sample 314-1b suggests that the dominant HMC phase with a $MgCO_3$ content
326 corresponding to about $2\theta = 13.6°$ is accompanied by some LMC, HMC, or even weakly
327 ordered dolomite with lower or higher $MgCO_3$ content, respectively (Fig. 5). The PXRD
328 profiles consequently reveal that the carbonates are not well-defined LMC, HMC, or
329 dolomite, but Ca-Mg carbonates with a nearly continuous spectrum of $MgCO_3$ contents.
330 The main (10.4) peaks of the Shenhu area Ca-Mg carbonates are more close to that of the
331 stoichiometric dolomite than those of the SW Taiwan basin Ca-Mg carbonates, which is
332 reflected in the higher $MgCO_3$ contents of the former.
333 The [010]-zone axis SAED patterns of the SW Taiwan basin Ca-Mg carbonate sample
334 314-1 show only weak superstructure reflections compared to the Shenhu area Ca-Mg

carbonates (Fig. 6). Because the superstructure reflections of dolomite patterns are caused by the substitution of Ca^{2+} layers by Mg^{2+} layers in the calcite structure (Fig. A1), the SAED patterns indicate that the 314-1 sample contains fewer Mg^{2+} layers than the Shenhu area samples. More details on the crystal structure become apparent from the in-situ FFT results obtained from the HRTEM images. The dolomite structure of Shenhu Ca-Mg carbonates is rather homogeneous, whereas only some micro-areas of the Taiwan basin carbonate reveal superstructure reflections (Fig. 7). The deficient $MgCO_3$ is scattered in the crystal lattice of the latter carbonate, representing a metastable structure with irregularly distributed $CaCO_3$ and $MgCO_3$ units. The additional reflections in the FFT patterns are best explained as c reflections (cf. Gunderson and Wenk, 1981; Van Tendeloo et al., 1985; Miser et al., 1987; Wenk et al., 1991; Schubel et al., 2000; Larsson and Christy, 2008; Shen et al., 2013). For a long time such reflections were believed to be derived from γ and ν carbonates with special arrangements of Ca^{2+} and Mg^{2+} layers (Van Tendeloo et al., 1985; Wenk and Zhang, 1985; Tsipursky and Buseck, 1993; Reeder, 2000). Recent work, however, indicated that the c reflection may originate from the multiple diffraction of dolomite and twinned calcite with similar cell parameters (Larsson and Christy, 2008; Shen et al., 2013). In the studied samples (Fig. 8), the dark contrast in micro-areas with c reflection suggests a local change in composition, which is probably due to a dominance of $CaCO_3$ units (cf. Gunderson and Wenk, 1981; Reeder, 1981; Wenk and Zhang, 1985; Miser et al., 1987; Reeder, 2000; Shen et al., 2013). Moreover, the

355 overlapping of the [010]-zone axis reflection patterns of calcite and dolomite with that of
356 (10.4) twinning calcite reveals similar patterns as those observed in the studied samples
357 (Fig. 8 and Fig. A3). Therefore, the c reflection in the samples is most probably caused
358 by multiple diffraction of the host dolomite or Mg-calcite and (10.4) twinned
359 nano-Mg-calcite.

360 To sum up, although the dominant carbonate phases are dolomite in the Shenhu area
361 samples and HMC and weakly ordered dolomite in SW Taiwan basin samples, all studied
362 samples must be considered as Ca-Mg carbonates with a wide range of $MgCO_3$ contents
363 and small scale inhomogeneities. The composition and the structure of Shenhu area
364 dolomites are close to stoichiometric dolomite, whereas the weakly ordered dolomite of
365 the SW Taiwan basin sample is typified by heterogeneously distributed micro-domains of
366 Ca-Mg carbonates, resulting in unevenly distributed microstructures and twinning.

367

368 **Conditions during the precipitation of seep carbonates**

369 The conditions during the precipitation of carbonates at methane seeps are indicated by
370 REE patterns and $\delta^{13}C$ values (e.g. Roberts et al., 2010; Birgel et al., 2011). The dynamic
371 nature of seepage activity impacts the precipitation conditions of carbonate minerals due
372 to changes of pore water composition in the course of changing fluid flux (e.g. Solomon
373 et al., 2008). Since the bottom water of the SCS is oxic, while the pore water at seeps is
374 anoxic (Alibo and Nozaki, 2000; Bayon et al., 2011), the minor but variable influence of

seawater on the precipitation of seep carbonates is reflected in their Ce anomalies (Feng et al., 2009a, 2009b, 2010; Birgel et al., 2011). Changes in the Ce distribution, and thus in the redox conditions during mineral formation, were even identified in different growth zones of individual carbonate minerals (Himmler et al., 2010). The relative contribution of seawater to the pore water in which precipitation takes place is also reflected in the ratios of LREE versus HREE. Seep carbonates precipitated from pore water reveal higher ratios than those of seawater (Himmler et al., 2013), which is reflected by Nd_N/Yb_N ratios (Fig. A2). Changes of seepage intensity, on the other hand, also have an impact on the carbon sources of seep carbonates. Methane contained in pore waters ($\delta^{13}C < -30‰$), seawater-derived dissolved inorganic carbon ($\delta^{13}C = 0‰$), and organic matter ($\delta^{13}C = \sim -25‰$) are the dominant carbon sources of carbonate minerals at seeps (e.g. Peckmann and Thiel, 2004; Roberts et al., 2010). If the relative influence of seawater on the environment of carbonate precipitation is low, i.e. in reducing pore waters shaped by methane oxidation, the $\delta^{13}C_{carbonate}$ values will be at the lower end.

The REE patterns of the studied SCS seep carbonates are similar to those of pore water (Fig. 9 and A1), indicating that precipitation occurred at greater sediment depth within pore waters largely different from seawater. Still, the Ce/Ce^* and Nd_N/Yb_N ratios of Shenhu area and SW Taiwan basin carbonates are different, pointing to differences in the conditions during precipitation (Table 3). By plotting against Pr/Pr^* ratios, real positive or negative Ce anomalies can be identified (Bau and Dulski, 1996). The majority of analyses

of the SW Taiwan basin sample revealed no Ce anomaly, while all Shenhu area samples exhibit real positive Ce anomalies (Fig. 10), pointing to anoxic conditions during carbonate formation. All studied carbonates precipitated from pore waters that were less oxidizing than seawater, but the formation environment was more reducing in the case of the Shenhu area Ca-Mg carbonates than in the case of the SW Taiwan basin carbonates. The obtained Nd_N/Yb_N ratios support this scenario. The Nd_N/Yb_N ratios increase from the SW Taiwan basin to the Shenhu area samples (Fig. 11b) and even reach beyond values typically observed for pore waters (approximately 1.2, Bayon et al., 2011). Cerium anomalies and the Nd_N/Yb_N ratios consequently both indicate that the Ca-Mg carbonates precipitated from anoxic pore waters impacted by SD-AOM, yet, the SW Taiwan basin carbonate formed under less reducing conditions than the Shenhu area carbonates.

The ^{13}C depletion of the SCS carbonates confirms their origin from methane oxidation. The somewhat higher $\delta^{13}C$ values of the SW Taiwan basin sample is probably the result of a more pronounced incorporation of carbon from sources other than methane including dissolved inorganic carbon from seawater and organic matter, although it is not possible to exclude that the observed pattern is caused by higher $\delta^{13}C$ values of parent methane from the SW Taiwan basin.

Formation of authigenic Ca-Mg carbonates at cold seeps

414 The compositions of Ca-Mg carbonates apparently change as a function of the redox
415 conditions of pore fluids as outlined above, with the $MgCO_3$ content positively correlated
416 with more reducing conditions. To illustrate such correlation, the Mg/Ca ratios of
417 carbonate phases are plotted against Ce/Ce^* and Nd_N/Yb_N ratios as well as $\delta^{13}C$ values
418 (Figs. 11 and 12). The positive trends in Mg/Ca versus Ce/Ce^* and Nd_N/Yb_N plots and the
419 negative trends in the Mg/Ca versus $\delta^{13}C$ value plots indicate that more Mg^{2+} ions are
420 incorporated into the Ca-Mg carbonates when the environment is more reducing and, thus,
421 more influenced by SD-AOM.

422 In a seawater environment with high Mg/Ca ratios, the precipitation of dolomite is
423 inhibited by the strong hydration of Mg^{2+} ions (Lippmann, 1973; Brady et al., 1996; Land,
424 1998; de Leeuw, 2002; Machel, 2004). However, dolomite formation is feasible in
425 methane-seep environments (e.g. Peckmann et al., 1999; Magalhães et al., 2012; Lu et al.,
426 2015). SD-AOM impacts the local conditions by converting methane and sulfate into
427 bicarbonate and sulfide (Boetius et al., 2000). Likewise, high concentrations of dissolved
428 inorganic carbon, sulfide, and the presence of EPS are able to catalyze the dehydration of
429 Mg^{2+} ions and facilitate the precipitation of dolomite (cf. Zhang et al., 2012a, 2012b,
430 2013; Shen et al., 2014, 2015). Dissolved carbonate ions are believed to be capable of
431 bonding with Mg^{2+} ions and enter the lattice of carbonate minerals (Lippmann, 1973;
432 Compton, 1988; Rushdi et al., 1992; Mazzullo, 2000). When present, sulfide will be
433 adsorbed on the growing surface of Ca-Mg carbonates and decrease the energy for

434 dehydration of Mg^{2+} ions, promoting the precipitation of Ca-Mg carbonates (Zhang et al.,
435 2012a). This relationship was recognized by atomic force microscopy (AFM; Zhang et al.,
436 2013) and confirmed by modelling (Shen et al., 2014). The effect of EPS – made of
437 carboxymethyl cellulose, agar, oligosaccharide, and glucose among other organic
438 molecules – on dolomite formation is similar to that of sulfide (Zhang et al., 2012b;
439 Zhang et al., 2014; Shen et al., 2015). Both being prominent in SD-AOM environments
440 (Boetius et al., 2000; Reitner et al., 2005; Treude et al., 2005), sulfide and EPS are likely
441 candidates to catalyze dolomite formation (Zhang et al., 2012a, 2012b, 2013, 2015; Shen
442 et al., 2014, 2015). The trends that become apparent in Fig. 11 and Fig. 12 can be
443 explained along the same lines. It is remarkable that the $MgCO_3$ content of Ca-Mg
444 carbonates is positively correlated with the presence and concentration of known catalysts
445 of dolomite formation (cf. Zhang et al., 2012a, 2012b, 2015). Since sulfide ions and ^{13}C
446 depleted carbonate species are simultaneously released by SD-AOM, negative $\delta^{13}C$
447 values correlate with high $MgCO_3$ contents in the precipitated Ca-Mg carbonates. Most of
448 the studied samples from the SCS fully conform to such a relationship, except for some
449 of the sub-samples of sample 4a-2 that yielded slightly higher $\delta^{13}C$ values (see Fig. 12).
450 Small and scattered pyrite crystals are only found in this sample (Fig. 3d), suggesting that
451 organoclastic sulfate reduction (OSR) may have been prominent at this site (cf. Lin et al.,
452 2016) and may have contributed to carbonate formation. The combination of sulfide and
453 EPS catalyses and the incorporation of some carbonate derived from OSR may have

454 resulted in the high $MgCO_3$ content but slightly less ^{13}C-depleted Ca-Mg carbonates in
455 this case.

456 Newly synthesized disordered dolomites are known to consist of nano-crystals, which
457 have low-angle grain boundaries among each other (Zhang et al., 2012a, 2012b, 2015).
458 The weakly ordered dolomite and dolomite in the SCS seep carbonates, however, are
459 characterized by relatively ordered anhedral to sub-euhedral crystals about 1 μm in
460 diameter. Since the conditions, such as alkalinity and initial Mg/Ca ratios, that have been
461 used in the experiments of Zhang et al. (2012a, 2012b, 2015) are similar to those
462 encountered at seeps (Gieskes et al., 2005; Yang et al., 2008; Wu et al., 2013), the
463 initially precipitated Ca-Mg carbonates should have been similar to their synthetic
464 counterparts. Accordingly, nano-crystals of the seep Ca-Mg carbonates may have been
465 crystallized from precursor clusters (cf. Gebauer et al., 2008; Gebauer and Cölfen, 2011;
466 Wallace et al., 2013) or amorphous phases (cf. Nielsen et al., 2014a; Raiteri and Gale,
467 2010; Quigley et al., 2011; Nielsen et al., 2014b; Wolf et al., 2008) by particle attachment
468 (cf. De Yoreo et al., 2015) under conditions of pronounced supersaturation generated by
469 SD-AOM. The $MgCO_3$ content of the nano-crystals likely was positively correlated to the
470 concentration of sulfide and the presence of EPS, which are closely correlated to the
471 intensity of SD-AOM and the supply of methane. The primarily disordered nano-crystals
472 apparently continued to grow, possibly by oriented attachment as has been observed for
473 titania (Lee Penn and Banfield, 1998). Subsequently the crystallographic barrier of

ordering was overcome (Xu et al., 2013), perhaps, by dissolution-crystallization reactions (Deelman, 2011; Pimentel and Pina, 2014) or recrystallization (Nordeng and Sibley, 1994; Kaczmarek et al., 2017). The cations became gradually ordered (see Fig. 13 for the envisioned scenario). The observed (10.4) twins of nano-crystals between neighboring Mg-calcite domains or between Mg-calcite and dolomite domains might form through an attachment mechanism (cf. De Yoreo et al., 2015; Lee Penn and Banfield, 1998) or cation ordering (cf. Shen et al., 2013). For Ca-Mg carbonates like those from the Shenhu area seeps that contain high enough $MgCO_3$ contents and are relatively old (~200 ka, Tong et al., 2013), the structure will predominantly evolve into stoichiometric, ordered dolomite. Only a few domains in the carbonates developed into Mg-calcite, some of which are (10.4) twinned with the dolomite host. In contrast, Ca-Mg carbonates with lower $MgCO_3$ contents and of a younger age (~70 ka, Tong et al., 2013) like the SW Taiwan carbonates will tend to exhibit only small and isolated dolomite domains, resulting in a more heterogeneous microstructure (Fig. 7 and 13) and (10.4) twins between Mg-calcite and the dolomite host as well as between neighboring Mg-calcite domains.

IMPLICATIONS

The "dolomite problem" has not lost much of its significance, despite of an improved understanding of the factors that impair dolomite formation at low temperatures. Recent laboratory and modelling studies indicate that disordered dolomite may precipitate at low

494 temperatures by catalysis (Zhang et al., 2012a, 2012b, 2015; Shen et al., 2014, 2015). Our
495 study lends support to this 'catalysis scenario', providing evidence from natural
496 environments that high levels of dissolved sulfide and EPS are capable of inducing
497 dolomite formation. A positive correlation between $MgCO_3$ contents, cerium anomalies,
498 Nd_N to Yb_N ratios, and ^{13}C-depletion suggests that Mg^{2+} ion incorporation into the crystal
499 lattice is favored by strongly reducing conditions caused by pronounced SD-AOM,
500 agreeing with catalytic dolomite formation induced by (1) SD-AOM derived sulfide and
501 (2) EPS produced by the SD-AOM consortium. Although the crystal morphologies and
502 the degree of ordering of the studied seep carbonates from the SCS are different from
503 those of synthetic disordered dolomite (Zhang et al., 2012a, 2012b, 2015), the latter could
504 still be an ideal analog for the natural samples if the effects of aging are to be considered
505 (cf. Hardie, 1987). Since sulfate is continuously supplied from seawater, the amount of
506 methane transported by seeps is critical for the extent of SD-AOM. Therefore, the overall
507 $MgCO_3$ contents of the authigenic carbonates from different seep sites are a constraint on
508 methane supply and cold seep activity. Future work will have to target dolomite of
509 variable ages from modern seeps and compare it to dolomite from ancient seep deposits.
510 It will also be insightful to compare dolomite resulting from SD-AOM with dolomite
511 resulting from OSR. Although both processes should be capable of inducing catalytic
512 dolomite formation, differences between SD-AOM and OSR derived dolomite may
513 provide further insight and contribute to the disentangling of the dolomite problem.

514

515 **ACKNOWLEDGMENTS**

516 This work was made possible by joint support from the Natural Science Foundation of
517 China (No. 91128101, 41273054, 41606063), the China Geological Survey Project for
518 South China Sea Gas Hydrate Resource Exploration (No.DD20160211), the National 127
519 Project (No.GZH201100305-06-04), Fundamental Research Funds for the Central
520 Universities (No.16lgjc11), and Guangdong Province Universities and Colleges Pearl
521 River Scholar Funded Scheme (No. 2011). Yang Lu also thanks the China Postdoctoral
522 Science Foundation (No. 2016M592565) and the Guangzhou Elite Project (No.
523 JY201223). Zhiyong Lin acknowledges the financial support from China Scholarship
524 Council (CSC; No. 201506380046). Huifang Xu acknowledges the support from NASA
525 Astrobiology Institute (07-5489) and National Science Foundation (EAR-095800,
526 DMR-0619368) of USA. We appreciate the samples provided and valuable suggestions
527 made by Shengxiong Yang, Guangxue Zhang, and Jinqiang Liang of the Guangzhou
528 Marine Geological Survey. Zhizhang Shen and Fangfu Zhang helped with the preparation
529 of TEM samples and the interpretation of data. This work benefited from the comments
530 of associate editor Alejandro Fernandez-Martinez, Prof.Jay M. Gregg, and an anonymous
531 reviewer.

532

533 **REFERENCES CITED**

534 Alibo, D.S., and Nozaki, Y. (2000) Dissolved rare earth elements in the South China Sea:
535 Geochemical characterization of the water masses. Journal of Geophysical
536 Research: Oceans, 105, 28771-28783.
537 Ayllón-Quevedo, F., Souza-Egipsy, V., Sanz-Montero, M.E., and Rodríguez-Aranda, J.P.
538 (2007) Fluid inclusion analysis of twinned selenite gypsum beds from the
539 Miocene of the Madrid basin (Spain). Implication on dolomite bioformation.
540 Sedimentary Geology, 201, 212-230.
541 Baker, P.A., and Kastner, M. (1981) Constraints on the formation of sedimentary
542 dolomite. Science, 213, 214-216.
543 Bau, M., and Dulski, P. (1996) Distribution of yttrium and rare-earth elements in the
544 Penge and Kuruman iron-formations, Transvaal Supergroup, South Africa.
545 Precambrian Research, 79, 37-55.
546 Bayon, G., Birot, D., Ruffine, L., Caprais, J.C., Ponzevera, E., Bollinger, C., Donval, J.P.,
547 Charlou, J.L., Voisset, M., and Grimaud, S. (2011) Evidence for intense REE
548 scavenging at cold seeps from the Niger Delta margin. Earth and Planetary
549 Science Letters, 312, 443-452.
550 Birgel, D., Feng, D., Roberts, H.H., and Peckmann, J. (2011) Changing redox conditions
551 at cold seeps as revealed by authigenic carbonates from Alaminos Canyon,
552 northern Gulf of Mexico. Chemical Geology, 285, 82-96.
553 Boetius, A., Ravenschlag, K., Schubert, C.J., Rickert, D., Widdel, F., Gieseke, A., Amann,
554 R., Jørgensen, B.B., Witte, U., and Pfannkuche, O. (2000) A marine microbial
555 consortium apparently mediating anaerobic oxidation of methane. Nature, 407,
556 623-626.
557 Borowski, W.S., Paull, C.K., and Ussler III, W. (1999) Global and local variations of
558 interstitial sulfate gradients in deep-water, continental margin sediments:
559 Sensitivity to underlying methane and gas hydrates. Marine Geology, 159,
560 131-154.
561 Brady, P.V., Krumhansl, J.L., and Papenguth, H.W. (1996) Surface complexation clues to
562 dolomite growth. Geochimica et Cosmochimica Acta, 60, 727-731.
563 Burns, S.J., McKenzie, J.A., and Vasconcelos, C. (2000) Dolomite formation and
564 biogeochemical cycles in the Phanerozoic. Sedimentology, 47, 49-61.
565 Chen, S., He, Z., He, J., Zhu, M., Chen, X., Pang, X., Weng, R., Cui, S., and Jiang, J.
566 (2009) The characters of the mud volcanoes in the north-east marginal of the
567 South China Sea and the relationship with the accumulation and migration of oil
568 and gas. Natural Gas Geoscience, 20, 872-878 (In Chinese with English abstract).
569 Compton, J.S. (1988) Degree of supersaturation and precipitation of organogenic
570 dolomite. Geology, 16, 318-321.
571 de Leeuw, N.H. (2002) Surface structures, stabilities, and growth of magnesian calcites: a
572 computational investigation from the perspective of dolomite formation.
573 American Mineralogist, 87, 679-689.

de Leeuw, N.H., and Parker, S.C. (2001) Surface-water interactions in the dolomite problem. Physical Chemistry Chemical Physics, 3, 3217-3221.

De Yoreo, J.J., Gilbert, P.U.P.A., Sommerdijk, N.A.J.M., Penn, R.L., Whitelam, S., Joester, D., Zhang, H., Rimer, J.D., Navrotsky, A., Banfield, J.F. and others (2015) Crystallization by particle attachment in synthetic, biogenic, and geologic environments. Science, 349, aaa6760.

Deelman, J.C. (2011) Low-temperature formation of dolomite and magnesite. Version 2.3, p. 512. http://www.jcdeelman.demon.nl/dolomite/bookprospectus.html.

Feng, D., and Chen, D. (2015) Authigenic carbonates from an active cold seep of the northern South China Sea: new insights into fluid sources and past seepage activity. Deep Sea Research II, 122, 74-83.

Feng, D., and Roberts, H.H. (2010) Initial results of comparing cold-seep carbonates from mussel- and tubeworm-associated environments at Atwater Valley lease block 340, northern Gulf of Mexico. Deep-Sea Research II, 57, 2030-2039.

Feng, D., Chen, D., and Peckmann, J. (2009a) Rare earth elements in seep carbonates as tracers of variable redox conditions at ancient hydrocarbon seeps. Terra Nova, 21, 49-56.

Feng, D., Chen, D., and Roberts, H.H. (2009b) Petrographic and geochemical characterization of seep carbonate from Bush Hill (GC 185) gas vent and hydrate site of the Gulf of Mexico. Marine and Petroleum Geology, 26, 1190-1198.

Feng, D., Chen, D., Peckmann, J., and Bohrmann, G. (2010) Authigenic carbonates from methane seeps of the northern Congo fan: Microbial formation mechanism. Marine and Petroleum Geology, 27, 748-756.

Feng, D., Peng, Y., Bao, H., Peckmann, J., Roberts, H.H., and Chen, D. (2016) A carbonate-based proxy for sulfate-driven anaerobic oxidation of methane. Geology, 44, 999-1002.

Fenter, P., Zhang, Z., Park, C., Sturchio, N.C., Hu, X.M., and Higgins, S.R. (2007) Structure and reactivity of the dolomite (104)-water interface: new insights into the dolomite problem. Geochimica et Cosmochimica Acta, 71, 566-579.

Ferrell, R.E., and Aharon, P. (1994) Mineral assemblages occurring around hydrocarbon vents in the northern Gulf of Mexico. Geo-Marine Letters, 14, 74-80.

Gebauer, D., and Cölfen, H. (2011) Prenucleation clusters and non-classical nucleation. Nano Today, 6, 564-584.

Gebauer, D., Völkel, A., and Cölfen, H. (2008) Stable prenucleation calcium carbonate clusters. Science, 322, 1819-1822.

Gieskes, J., Mahn, C., Day, S., Martin, J.B., Greinert, J., Rathburn, T., and McAdoo, B. (2005) A study of the chemistry of pore fluids and authigenic carbonates in methane seep environments: Kodiak Trench, Hydrate Ridge, Monterey Bay, and Eel River Basin. Chemical Geology, 220, 329-345.

Goldsmith, J.R., and Graf, D.L. (1958) Relation between lattice constants and composition of the Ca-Mg carbonates. American Mineralogist, 43, 84-101.

615 Gong, Y., Yang, S., Wang, H., Liang, J., Guo, Y., Wu, S., and Liu, G. (2009) Gas hydrate
616 reservoir characteristics of Shenhu area, north slope of the South China Sea.
617 Geoscience, 23, 210-216 (In Chinese with English abstract).
618 Graf, D.L. (1961) Crystallographic tables for the rhombohedral carbonates. American
619 Mineralogist, 46, 1283-1316.
620 Gregg, J.M., Bish, D.L., Kaczmarek, S.E., and Machel, H.G. (2015) Mineralogy,
621 nucleation and growth of dolomite in the laboratory and sedimentary environment:
622 A review. Sedimentology, 62, 1749-1769.
623 Greinert, J., Bohrmann, G, Suess, E. (2001) Gas hydrate-associated carbonates and
624 methane-venting at Hydrate Ridge: classification distribution and origin of
625 authigenic lithologies. In C.K. Paull, and P.W. Dillon, Eds. Natural gas hydrates:
626 Occurrence, distribution, and detection, 124, p. 99-113. Geophysical Monograph.
627 Gunderson, S.H., and Wenk, H.R. (1981) Heterogeneous microstructures in oolitic
628 carbonates. American Mineralogist, 66, 789-800.
629 Haas, A., Peckmann, J., Elvert, M., Sahling, H., and Bohrmann, G. (2010) Patterns of
630 carbonate authigenesis at the Kouilou pockmarks on the Congo deep-sea fan.
631 Marine Geology, 268, 129-136.
632 Han, X., Suess, E., Huang, Y., Wu, N., Bohrmann, G., Su, X., Eisenhauer, A., Rehder, G.,
633 and Fang, Y. (2008) Jiulong methane reef: Microbial mediation of seep
634 carbonates in the South China Sea. Marine Geology, 249, 243-256.
635 Hardie, L.A. (1987) Dolomitization: a critical view of some current views. Journal of
636 Sedimentary Petrology, 57, 166-183.
637 Higgins, S.R., and Hu, X.M. (2005) Self-limiting growth on dolomite: Experimental
638 observations with in situ atomic force microscopy. Geochimica et Cosmochimica
639 Acta, 69, 2085-2094.
640 Himmler, T., Bach, W., Bohrmann, G., and Peckmann, J. (2010) Rare earth elements in
641 authigenic methane-seep carbonates as tracers for fluid composition during early
642 diagenesis. Chemical Geology, 277, 126-136.
643 Himmler, T., Haley, B.A., Torres, M.E., Klinkhammer, G.P., Bohrmann, G., and
644 Peckmann, J. (2013) Rare earth element geochemistry in cold-seep pore waters of
645 Hydrate Ridge, northeast Pacific Ocean. Geo-Marine Letters, 33, 369-379.
646 Hu, X.M., Grossie, D.A., and Higgins, S.R. (2005) Growth and dissolution kinetics at the
647 dolomite-water interface: an in-situ scanning probe microscopy study. American
648 Mineralogist, 90, 963-968.
649 Hu, Y., Feng, D., Peckmann, J., Roberts, H.H., and Chen, D. (2014) New insights into
650 cerium anomalies and mechanisms of trace metal enrichment in authigenic
651 carbonate from hydrocarbon seeps. Chemical Geology, 381, 55-66.
652 Huang, C., Chien, C., Zhao, M., Li, H., and Lizuka, Y. (2006) Geological study of active
653 cold seeps in the syn-collision accretionary prism Kaoping slope off SW Taiwan.
654 Terrestrial Atmospheric and Oceanic Sciences 17, 679-702.

Huang, Y., Suess, E., and Wu, N. (2008) Methane and gas hydrate geology in the northern slope of the South China Sea. Special report for Sino-German cooperative SO-177 cruise. Geological Publishing House, Beijing (In Chinese).

Kaczmarek, S.E., Gregg, J.M., Bish, D.L., Machel, H.G., and Fouke, B.W. (2017) Dolomite, very high-magnesium calcite, and microbes—Implications for the microbial model of dolomitization. SEPM Special Publication, 109, 1-14.

Land, L.S. (1998) Failure to precipitate dolomite at 25°C from dilute solution despite 1000-fold oversaturation after 32 years. Aquatic Geochemistry, 4, 361-368.

Larsson, A.-K., and Christy, A.G. (2008) On twinning and microstructures in calcite and dolomite. American Mineralogist, 93, 103-113.

Lee Pen, R., and Banfield, J.F. (1998) Imperfect oriented attachment: Dislocation generation in defect-free nanocrystals. Science, 281, 969-971.

Liebermann, O. (1967) Synthesis of dolomite. Nature, 21, 241-245.

Lin, Z., Sun, X., Lu, Y., Strauss, H., Xu, L., Gong, J., Teichert, B.M.A., Lu, R., Lu, H., Sun, W., and Peckmann, J. (2017a) The enrichment of heavy iron isotopes in authigenic pyrite as a possible indicator of sulfate-driven anaerobic oxidation ofmethane: Insights from the South China Sea. Chemical Geology, 449, 15-29.

Lin, Z., Sun, X., Peckmann, J., Lu, Y., Xu, L., Strauss, H., Zhou, H., Gong, J., Lu, H., and Teichert, B.M.A. (2016) How sulfate-driven anaerobic oxidation of methane affects the sulfur isotopic composition of pyrite: a SIMS study from the South China Sea. Chemical Geology, 440, 26-41.

Lin, Z., Sun, X., Strauss, H., Lu, Y., Gong, J., Xu, L., Lu, H., Teichert, B.M.A., and Peckmann, J. (2017b) Multiple sulfur isotope constraints on sulfate-driven anaerobic oxidation of methane: Evidence from authigenic pyrite in seepage areas of the South China Sea. Geochimica et Cosmochimica Acta, 211, 153-173.

Lippmann, F. (1973) Sedimentary Carbonate Minerals. 228 p. Springer-Verlag, Berlin and New York.

Lu, Y., Liu, Y., Sun, X., Lin Z., Xu, L., Lu, H., Hao, X., Peckmann, J. (2017) Intensity of methane seepage reflected by relative enrichment of heavy magnesium isotopes in authigenic carbonates: A case study from the South China Sea. Deep-Sea Research Part I, http://dx.doi.org/10.1016/j.dsr.2017.09.005.

Lu, Y., Sun, X., Lin, Z., Xu, L., Gong, J., and Lu, H. (2015) Cold seep status archived in authigenic carbonates: Mineralogical and isotopic evidence from Northern South China Sea. Deep-Sea Research II, 122, 95-105.

Machel, H.G. (2004) Concepts and models of dolomitization: a critical reappraisal. In C.J.R. Braithwaite, G. Rizzi, and G. Darke, Eds. The Geometry and Petrogenesis of Dolomite Hydrocarbon Reservoirs, 235, p. 7-63. Geological Society, London.

Magalhães, V.H., Pinheiro, L.M., Ivanov, M.K., Kozlova, E., Blinova, V., Kolganova, J., Vasconcelos, C., McKenzie, J.A., Bernasconi, S.M., Kopf, A.J., Díaz-del-Río, V., Javier González, F., and Somoza, L. (2012) Formation processes of

methane-derived authigenic carbonates from the Gulf of Cadiz. Sedimentary Geology, 243, 155-168.

Markgraf, S.A., and Reeder, R.J. (1985) High-temperature structure refinements of calcite and magnesite. American Mineralogist, 70, 590-600.

Mazzullo, S. (2000) Organogenic dolomitization in peritidal to deep-sea sediments. Journal of Sedimentary Research, 70, 10-23.

McLennan, S.M. (1989) Rare earth elements in sedimentary rocks: Influence of provenance and sedimentary processes. In B.R. Lipin, and G.A. McKay, Eds. Geochemistry and Mineralogy of Rare Earth Elements. Reviews in Mineralogy, 21, p. 169-200.

Miser, D.E., Swinnea, J.S., and Steinfink, H. (1987) TEM observations and X-ray crystal-structure refinement of a twinned dolomite with a modulated microstructure. American Mineralogist, 72, 188-193.

Nielsen, M.H., Aloni, S., and De Yoreo, J.J. (2014a) In situ TEM imaging of $CaCO_3$ nucleation reveals coexistence of direct and indirect pathways. Science, 345, 1158-1162.

Nielsen, M.H., Li, D., Zhang, H., Aloni, S., Han, T.Y., Frandsen, C., Seto, J., Banfield, J.F., Cölfen, H., and De Yoreo, J.J. (2014b) Investigating processes of nanocrystal formation and transformation via liquid cell TEM. Microscopy and Microanalysis, 20, 425-436.

Nordeng, S.H., and Sibley, D.F. (1994) Dolomite stoichiometry and Ostwald's Step Rule. Geochimica et Cosmochimica Acta, 58, 191-196.

Pang, X., Chen, C., Zhu, M., He, M., Shen, J., and Liu, B. (2006) A discussion about hydrocarbon accumulation conditions in Baiyun Deep-water Area, the northern continental slope, South China Sea. China Offshore Oil and Gas, 18, 145-149 (In Chinese with English abstract).

Peckmann, J., and Thiel, V. (2004) Carbon cycling at ancient methane-seeps. Chemical Geology, 205, 443-467.

Peckmann, J., Birgel, D., and Kiel, S. (2009) Molecular fossils reveal fluid composition and flow intensity at a Cretaceous seep. Geology, 37, 847-850.

Peckmann, J., Thiel, V., Michaelis, W., Clari, P., Gaillard, C., Martire, L., and Reitner, J. (1999) Cold seep deposits of Beauvoisin (Oxfordian; southeastern France) and Marmorito (Miocene; northern Italy): microbially induced authigenic carbonates. International Journal of Earth Sciences, 88, 60-75.

Perri, E., and Tucker, M. (2007) Bacterial fossils and microbial dolomite in Triassic stromatolites. Geology, 35, 207-210.

Pimentel, C., and Pina, C.M. (2014) The formation of the dolomite-analogue norsethite: Reaction pathway and cation ordering. Geochimica et Cosmochimica Acta, 142, 217-223.

Pokrovsky, O.S. (1998) Precipitation of calcium and magnesium carbonates from homogeneous supersaturated solutions. Journal of Crystal Growth, 186, 233-239.

Quigley, D., Freeman, C.L., Harding, J.H., and Rodger, P.M. (2011) Sampling the structure of calcium carbonate nanoparticles with metadynamics. The Journal of Chemical Physics, 134, 044703.

Reeder, R. (1981) Electron optical investigation of sedimentary dolomites. Contributions to Mineralogy and Petrology, 76, 148-157.

Reeder, R.J. (2000) Constraints on cation order in calcium-rich sedimentary dolomite. Aquatic Geochemistry, 6, 213-226.

Reitner, J., Peckmann, J., Reimer, A., Schumann, G., and Thiel, V. (2005) Methane-derived carbonate build-ups and associated microbial communities at cold seeps on the lower Crimean shelf (Black Sea). Facies, 51, 66-79

Riding, R. (2000) Microbial carbonates: the geological record of calcified bacterial-algal mats and biofilms. Sedimentology, 47, 179-214.

Rietveld, H.M. (1967) Line profiles of neutron powder-diffraction peaks for structure refinement. Acta Crystallographica, 22, 151-152.

Roberts, H.H., Feng, D., and Joye, S.B. (2010) Cold-seep carbonates of the middle and lower continental slope, northern Gulf of Mexico. Deep-Sea Research II, 57, 2040-2054.

Roberts, J.A., Bennett, P.C., González, L.A., Macpherson, G.L., and Milliken, K.L. (2004) Microbial precipitation of dolomite in methanogenic groundwater. Geology, 32, 277-280.

Romanek, C.S., Jimenez-Lopez, C., Rodriguez Navarro, A., Sanchez-Roman, M., Sahai, N., and Coleman, M. (2009) Inorganic synthesis of Fe-Ca-Mg carbonates at low temperature. Geochimica et Cosmochimica Acta, 73, 5361-5376.

Rushdi, A.I., Pytkowicz, R.M., Suess, E., and Chen, C.T. (1992) The effects of magnesium-to-calcium ratios in artificial seawater, at different ionic products, upon the induction time, and the mineralogy of calcium carbonate: a laboratory study. Geologische Rundschau, 81, 571-578.

Schubel, K.A., Elbert, D.C., and Veblen, D.R. (2000) Incommensurate c-domain superstructures in calcian dolomite from the Latemar buildup, Dolomites, Northern Italy. American Mineralogist, 85, 858-862.

Shen, Z., Konishi, H., Brown, P.E., and Xu, H. (2013) STEM investigation of exsolution lamellae and "c" reflections in Ca-rich dolomite from the Platteville Formation, western Wisconsin. American Mineralogist, 98, 760-766.

Shen, Z., Liu, Y., Brown, P.E., Szlufarska, I., and Xu, H. (2014) Modeling the effect of dissolved hydrogen sulfide on Mg^{2+}-water complex on dolomite {104} surfaces. The Journal of Physical Chemistry C, 118, 15716-15722.

Shen, Z., Szlufarska, I., Brown, P.E., and Xu, H. (2015) Investigation of the role of polysaccharide in the dolomite growth at low temperature by using atomistic simulations. Langmuir, 31, 10435-10442.

Solomon, E.A., Kastner, M., Jannasch, H., Robertson, G., and Weinstein, Y. (2008) Dynamic fluid flow and chemical fluxes associated with a seafloor gas hydrate

777 deposit on the northern Gulf of Mexico slope. Earth and Planetary Science Letters,
778 270, 95-105.
779 Suess, E. (2010) Marine cold seeps. In K.N. Timmis, Ed. Handbook of hydrocarbon and
780 Lipid Microbiology, 1, p. 187-203. Springer-Verlag, Berlin Heidelberg.
781 Suess, E. (2014) Marine cold seeps and their manifestations: geological control,
782 biogeochemical criteria and environmental conditions. International Journal of
783 Earth Sciences, 103, 1889-1916.
784 Sun, Q., Wu, S., Cartwright, J., and Dong, D. (2012a) Shallow gas and focused fluid flow
785 systems in the Pearl River Mouth Basin, northern South China Sea. Marine
786 Geology, 315-318, 1-14.
787 Sun, Y., Wu, S., Dong, D., Lüdmann, T., and Gong, Y. (2012b) Gas hydrates associated
788 with gas chimneys in fine-grained sediments of the northern South China Sea.
789 Marine Geology, 311-314, 32-40.
790 Tong, H., Feng, D., Cheng, H., Yang, S., Wang, H., Min, A.G., Edwards, R.L., Chen, Z.,
791 and Chen, D. (2013) Authigenic carbonates from seeps on the northern
792 continental slope of the South China Sea: new insights into fluid sources and
793 geochronology. Marine and Petroleum Geology, 43, 260-271.
794 Treude, T., Knittel, K., Blumenberg, M., Seifert, R., and Boetius, A. (2005) Subsurface
795 microbial methanotrophic mats in the Black Sea. Applied and Environmental
796 Microbiology, 71, 6375-6378.
797 Tsipursky, S.J., and Buseck, P.R. (1993) Structure of magnesian calcite from sea urchins.
798 American Mineralogist, 78, 775-781.
799 Van Lith, Y., Warthmann, R., Vasconcelos, C., and McKenzie, J.A. (2003a) Microbial
800 fossilization in carbonate sediments: a result of the bacterial surface involvement
801 in dolomite precipitation. Sedimentology, 50, 237-245.
802 Van Lith, Y., Warthmann, R., Vasconcelos, C., and McKenzie, J.A. (2003b)
803 Sulphate-reducing bacteria induce low-temperature Ca-dolomite and high
804 Mg-calcite formation. Geobiology, 1, 71-79.
805 Van Tendeloo, G., Wenk, H.R., and Gronsky, R. (1985) Modulated structures in calcian
806 dolomite: a study by electron microscopy. Physics and Chemistry of Minerals, 12,
807 333-341.
808 Vasconcelos, C., and McKenzie, J.A. (1997) Microbial mediation of modern dolomite
809 precipitation and diagenesis under anoxic conditions (Lagoa Vermelha, Rio de
810 Janeiro, Brazil). Journal of Sedimentary Research, 67, 378-390.
811 Wallace, A.F., Hedges, L.O., Fernandez-Martinez, A., Raiteri, P., Gale, J.D., Waychunas,
812 G.A., Whitelam, S., Banfield, J.F., and De Yoreo, J.J. (2013) Microscopic
813 evidence for liquid-liquid separation in supersaturated $CaCO_3$ solutions. Science,
814 341, 885-889.
815 Warren, J. (2000) Dolomite: occurrence, evolution and economically important
816 associations. Earth-Science Reviews, 52, 1-81.

Wasylenki, L.E., Dove, P.M., and De Yoreo, J.J. (2005) Effects of temperature and transport conditions on calcite growth in the presence of Mg^{2+}: Implications for paleothermometry. Geochimica et Cosmochimica Acta, 69, 4227-4236.

Wenk, H.R., and Zhang, F. (1985) Coherent transformations in calcian dolomites. Geology, 13, 457-460.

Wenk, H.R., Meisheng, H., Lindsey, T., and Morris, J.W., Jr. (1991) Superstructures in ankerite and calcite. Physics and Chemistry of Minerals, 17, 527-539.

Wolf, S.E., Leiterer, J., Kappl, M., Emmerling, F., and Tremel, W. (2008) Early homogenous amorphous precursor stages of calcium carbonate and subsequent crystal growth in levitated droplets. Journal of the American Chemical Society 130, 12342-12347.

Wright, D.T. (1999) The role of sulphate-reducing bacteria and cyanobacteria in dolomite formation in distal ephemeral lakes of the Coorong region, South Australia. Sedimentary Geology, 126, 147-157.

Wu, L., Yang, S., Liang, J., Su, X., Fu, S., Sha, Z., and Yang, T. (2013) Variations of pore water sulfate gradients in sediments as indicator for underlying gas hydrate in Shenhu Area, the South China Sea. Science China Earth Sciences, 56, 530-540.

Wu, N., Suess, E., Fu, S., Domeyer, B., Huang, Y., and Zhu, Y. (2006) Pore-water geochemistry of surface sediments from Haiyang 4 area of the northeastern South China Sea. Western Pacific Geophysics Meeting, EOS Trans. AGU Abstract, 87, OS31A-0098.

Xu, J., Yan, C., Zhang, F., Konishi, H., Xu, H., and Teng, H.H. (2013) Testing the cation-hydration effect on the crystallization of Ca-Mg-CO_3 systems. Proceedings of the National Academy of Sciences, 110, 17750-17755.

Yang, T., Jiang, S., Yang, J., Lu, G., Wu, N., Liu, J., and Chen, D. (2008) Dissolved inorganic carbon (DIC) and its carbon isotopic composition in sediment pore waters from the Shenhu area, northern South China Sea. Journal of Oceanography, 64, 303-310.

Yin, X., Zhou, H., Yang, Q., Wang, H., and Chen, J. (2008) The evidence for the existence of methane seepages in the northern South China Sea: abnormal high methane concentration in bottom waters. Acta Oceanologica Sinica, 27, 62-70.

Zenger, D.H., and Dunham, J.B. (1980) Concepts and models of dolomitization - an introduction. Society for Sedimentary Geology 28, 1-9.

Zhang, F., Xu, H., Konishi, H., and Roden, E.E. (2010) A relationship between d_{104} value and composition in the calcite-disordered dolomite solid-solution series. American Mineralogist, 95, 1650-1656.

Zhang, F., Xu, H., Konishi, H., Kemp, J.M., Roden, E.E., and Shen, Z. (2012a) Dissolved sulfide-catalyzed precipitation of disordered dolomite: Implications for the formation mechanism of sedimentary dolomite. Geochimica et Cosmochimica Acta, 97, 148-165.

Zhang, F., Xu, H., Konishi, H., Shelobolina, E.S., and Roden, E.E. (2012b) Polysaccharide-catalyzed nucleation and growth of disordered dolomite: A potential precursor of sedimentary dolomite. American Mineralogist, 97, 556-567.

Zhang, F., Xu, H., Shelobolina, E.S., Konishi, H., Converse, B., Shen, Z., and Roden, E.E. (2015) The catalytic effect of bound extracellular polymeric substances excreted by anaerobic microorganisms on Ca-Mg carbonate precipitation: Implications for the "dolomite problem". American Mineralogist, 100, 483-494.

Zhang, F., Yan, C., Teng, H.H., Roden, E.E., and Xu, H. (2013) In situ AFM observations of Ca-Mg carbonate crystallization catalyzed by dissolved sulfide: Implications for sedimentary dolomite formation. Geochimica et Cosmochimica Acta, 105, 44-55.

Zhu, Y., Huang, Y., Matsumoto, R., and Wu, B. (2003) Geochemical and stable isotopic compositions of pore fluids and authigenic siderite concretions from site 1146, ODP Leg 184: implication for gas hydrate. In W.L. Prell, P. Wang, P. Blum, D.K. Rea, and S.C. Clemens, Eds. Proceedings of the Ocean Drilling Program, Scientific Results, 184, p. 1-15.

875 **Figure captions**
876

877 **Figure 1.** Map of northern South China Sea. The Shenhu area and SW Taiwan basin are
878 highlighted by gray squares. Sites HS4 and HS4a from the Shenhu area and site 314 from
879 the SW Taiwan basin are indicated by red circles.

880

881 **Figure 2.** Photographs of authigenic carbonates. Red circles indicate spots where samples
882 have been taken. (a): Sub-sample of sample 4-1, polished surface revealing that the outer
883 part of the sample to the right is weathered. (b): Polished slab of sample 4-2. (c): Sample
884 4-3. (d): Polished surface of sample 4a-1, different degrees of weathering are revealed
885 from the near center to the rim of the sample. (e): Sub-sample of sample 4a-2, similar to
886 4a-1, the internal gray part reveals no signs of weathering. (f): Sample 314-1, the gray
887 part is apparently unaffected by weathering.

888

889 **Figure 3.** Photomicrographs of authigenic carbonates and enclosed pyrite aggregates. (a):
890 Sample 4-1, microcrystalline carbonate cementing detrital quartz, feldspar, and some
891 bioclasts. (b): Sample 314-1, microcrystalline carbonate enclosing detrital quartz,
892 feldspar, and some bioclasts, as well as minor authigenic pyrite (black). (c): Sample
893 314-1, partly oxidized framboidal pyrite, filling the chambers of a foraminifer. (d):
894 Sample 4a-2, unaltered pyrite crystals (arrows) and larger aggregates of framboidal pyrite
895 filling foraminifers scattered in carbonate matrix.

896

897 **Figure 4.** High-angle angular dark-field STEM images of microcrystalline authigenic
898 carbonates of samples 4a-2 (a), 4-3 (b), and 314-1 (c and d). The carbonate crystals are
899 sub-euhedral to anhedral in Shenhu samples (4a-2 and 4-3), while carbonate crystals of
900 314-1 are anhedral. Crystal size is about 1 μm. The interspace of carbonates is filled by
901 illite. Carb = HMC or dolomite; Ilt = illite.

902

903 **Figure 5.** Powder X-ray diffraction patterns of selected samples and calculated patterns
904 of Mg-free calcite (Markgraf and Reeder, 1985) and dolomite (Graf, 1961) and
905 characteristic diffractograms of identified phases. The superstructure reflections or
906 ordering reflections of dolomite, (01.–1*{note to typesetting, the minus sign is the overbar*
907 *on top of the 1}*) and (01.5), are shown in the diffractogram. The hump at around 2θ = 10°
908 is caused by the glass fiber. (10.4) peaks of carbonates are magnified on the right. The
909 peaks of samples are distributed between those of the Mg-free calcite and dolomite. This
910 region is divided into three sub-regions according to Lu et al. (2015). The sub-regions 1,
911 2, and 3 correspond to the (10.4) peaks of low-Mg calcite, high-Mg calcite, and dolomite,
912 respectively. Qz = quartz; Ab = albite; Or = orthoclase; Ilt = illite; Cal = Mg-calcite; Dol
913 = dolomite.

914

915 **Figure 6.** TEM images of selected carbonate minerals of samples 4a-2 (a), 4-3 (b and c),
916 and 314-1 (d). The insets are [010]-zone axis selected-area diffraction patterns and EDS
917 results. From a to d, the discrepancy between peak heights of Ca and Mg in EDS spectra
918 increases. Simultaneously, the intensity of the superstructure reflections becomes weaker.
919
920 **Figure 7.** HRTEM images and [010]-zone axis Fourier transformation patterns of
921 samples 4-3 (a to e) and 314-1 (f to t). Only a few domains show weak superstructure
922 reflections in sample 4-3 (a to e). In contrast, the analyzed carbonate minerals of sample
923 314-1 are composed of domains with dolomite or calcite structure (with or without
924 superstructure reflections). In some parts, the domains with these two structures are
925 almost equal (f to j). In other parts, micro-areas with the dolomite structure are
926 surrounded by areas with calcite structure (k to o) and vice versa (p to t).
927
928 **Figure 8.** High-resolution TEM images and [010]-zone axis Fourier transformation
929 patterns of samples 4a-2 (a and b), 4-3 (c and d), and 314-1 (e to h). Small domains with
930 dark contrast are apparent in all images. Additional reflection patterns, indicated by
931 arrows, occur at nearly half way between (00.0) to (10.4) reflections (b, f, and h) and
932 between (00.0) to (10.–2*{note to typesetting, the minus sign is the overbar on top of the*
933 *2}*) reflections (d). The additional reflections highlighted by yellow arrows are the c
934 reflections, while those pointed by white arrows are interpreted to be derived from the

multiple scattering of [10–2*{note to typesetting, the minus sign is the overbar on top of the 2}*] or [101] reflections from the host dolomite or Mg-calcite by the twinned nano-Mg-calcite.

Figure 9. Shale-normalized rare earth element patterns of the studied authigenic carbonates with middle REE bulge.

Figure 10. Plot of Ce/Ce^* vs. Pr/Pr^* of authigenic carbonates (after Bau and Dulski, 1996). Field 1: real positive Ce anomaly; Field 2: no anomaly; Field 3: real negative Ce anomaly.

Figure 11. Plots of Ce/Ce^* vs. Mg/Ca (mole ratio) (a) and Nd_N/Yb_N vs. Mg/Ca (b) of authigenic carbonates. The Ce/Ce^* and Nd_N/Yb_N ratios of seawater (SW, Alibo and Nozaki, 2000) and pore water (PW, Bayon et al., 2011) are indicated by blue and orange lines, respectively. Both plots reveal a positive trend to more reducing environments from seawater composition over the SW Taiwan sample (314) to the Shenhu samples (4 and 4a).

Figure 12. Diagram of $\delta^{13}C$ values vs. Mg/Ca (mole ratio). The red area represents marine non-seep carbonates. An indistinct negative trend is apparent from marine

non-seep carbonates over the SW Taiwan sample (314) to Shenhu samples (4 and 4a). The observed trend is suggested to be caused by the combined effects of sulfide catalysis and extracellular polymeric substances (EPS) catalysis.

Figure 13. Scenario for the formation of weakly ordered dolomite and dolomite in the authigenic seep carbonates induced by the catalysis of sulfate-driven anaerobic oxidation of methane (SD-AOM) derived sulfide and extracellular polymeric substances (EPS), involving particle attachment (cf. De Yoreo et al., 2015), and ordering caused by crystal maturation and recrystallization. Nano-crystals of Ca-Mg carbonates containing various amounts of $MgCO_3$ may be formed under the influence of sulfide and EPS catalysis from the attachment of precursor clusters or amorphous phases. The newly crystallized particles may continue to grow by oriented attachment. The cations are rearranged to form the dolomite structure during maturation and recrystallization as time passes by. Ca-Mg carbonates with insufficient $MgCO_3$, like the SW Taiwan basin sample (left), can only evolve some domains with a dolomite structure, while those with sufficient $MgCO_3$, such as Shenhu area samples (right), develop into nearly stoichiometric dolomite. (10.4) twins between nano-Mg-calcite and dolomite and between nano-Mg-calcite and Mg-calcite may also form.

This is a preprint, the final version is subject to change, of the American Mineralogist (MSA)
Cite as Authors (Year) Title. American Mineralogist, in press.
DOI: https://doi.org/10.2138/am-2018-6226

975 **Table 1.** Contents of major minerals and d_{104} values of carbonate minerals in the studied
976 authigenic carbonates.

Location	Sample	Qz	Ab	Or	Ilt	HMC	Dol	d_{104} HMC	d_{104} Dol
		(weight%)						(Å)	
Shenhu HS4	4-1	11.9	3.7	12.5	13.7	0.9	57.3	2.969	2.903
	4-2	19.5	3.7	6.4	14.4	2.2	53.8	2.966	2.911
	4-3	23.5	5.4	3.6	17.9	13.3	36.4	2.974	2.914
Shenhu HS4a	4a-1	13.5	3.2	9.5	14.1	1.2	58.5	2.981	2.914
	4a-2	14.4	3.3	5.2	20.2	1.4	55.5	2.975	2.905
SW Taiwan HD314	314-1a	19.8	6.6	2.1	11.5	59.3	0.7	2.992	2.934
	314-1b	8.9	3.5	5.2	15.7	51.0	15.7	2.999	2.926
	314-1c	9.1	6.8	7.8	13.8	25.8	36.6	2.995	2.930

Qz = quartz, Ab = albite, Or = orthoclase, Ilt = illite, HMC = high-Mg calcite, Dol = dolomite.

977

978

This is a preprint, the final version is subject to change, of the American Mineralogist (MSA)
Cite as Authors (Year) Title. American Mineralogist, in press.
DOI: https://doi.org/10.2138/am-2018-6226

979 **Table 2.** Contents of Ca and Mg, Mg/Ca ratios, and C and O isotope compositions of the
980 studied authigenic carbonates.

Location	Sample	Ca (%)	Mg (%)	Mg/Ca[a]	$\delta^{13}C$ (‰)	$\delta^{18}O$ (‰)
Shenhu HS4	4-1a	12.9	5.3	0.67	–44.8	3.4
	4-1b	12.7	3.9	0.50	–46.7	2.5
	4-2	13.3	4.5	0.56	–49.2	3.2
	4-3	13.0	3.9	0.50	–45.8	3.0
Shenhu HS4a	4a-1a	13.2	4.2	0.52	–47.7	3.4
	4a-1b	15.5	5.2	0.56	–47.5	3.5
	4a-2a	13.8	5.6	0.67	–39.2	3.1
	4a-2b	13.6	5.5	0.67	–36.9	2.7
SW Taiwan HD314	314-1a	18.5	3.2	0.28	–39.4	1.4
	314-1b	19.0	4.2	0.37	–37.6	1.5
	314-1c	18.7	3.5	0.31	–34.6	1.4
	314-1d	16.3	2.9	0.30	–27.7	1.4

[a]mole ratio.

981

This is a preprint, the final version is subject to change, of the American Mineralogist (MSA)
Cite as Authors (Year) Title. American Mineralogist, in press.
DOI: https://doi.org/10.2138/am-2018-6226

982 **Table 3.** Rare earth elements contents and selected element ratios of the studied authigenic carbonates.

Location	Sample	La	Ce	Pr	Nd	Sm	Eu	Gd	Tb	Dy	Ho	Er	Tm	Yb	Lu	ΣREE	Ce/Ce*	Pr/Pr*	Nd_N/Yb_N[a]
		(ppm)																	
	4-1a	3.45	8.92	0.917	3.74	0.839	0.165	0.799	0.101	0.593	0.0930	0.279	0.0330	0.233	0.0291	20.2	1.15	0.934	1.34
Shenhu	4-1b	3.62	9.03	0.918	3.84	0.863	0.178	0.853	0.105	0.637	0.103	0.311	0.0376	0.247	0.0336	20.8	1.14	0.918	1.29
HS4	4-2	3.78	9.45	0.988	4.06	0.911	0.177	0.881	0.109	0.670	0.105	0.314	0.0362	0.253	0.0342	21.8	1.13	0.937	1.33
	4-3	3.79	9.54	0.977	3.96	0.875	0.173	0.834	0.104	0.630	0.100	0.306	0.0353	0.239	0.0334	21.6	1.14	0.935	1.38
	4a-1a	3.90	9.67	1.00	4.09	0.911	0.178	0.877	0.108	0.650	0.100	0.304	0.0347	0.245	0.0347	22.1	1.13	0.937	1.39
Shenhu	4a-1b	3.95	9.95	1.03	4.24	0.921	0.188	0.882	0.112	0.650	0.103	0.312	0.0368	0.250	0.0348	22.7	1.13	0.936	1.41
HS4a	4a-2a	3.83	9.57	0.990	4.06	0.903	0.179	0.859	0.106	0.637	0.102	0.297	0.0346	0.235	0.0327	21.8	1.13	0.934	1.44
	4a-2b	3.78	9.53	0.988	3.99	0.904	0.175	0.851	0.105	0.644	0.102	0.288	0.0339	0.247	0.0320	21.7	1.13	0.943	1.35
	314-1a	2.99	6.90	0.760	3.26	0.740	0.168	0.756	0.0996	0.603	0.0977	0.299	0.0351	0.246	0.0352	17.0	1.05	0.941	1.10
SW	314-1b	2.95	6.63	0.763	3.17	0.729	0.169	0.741	0.0963	0.578	0.0944	0.283	0.0334	0.222	0.0354	16.5	1.02	0.978	1.19
Taiwan	314-1c	3.20	7.26	0.825	3.45	0.815	0.186	0.837	0.108	0.655	0.107	0.325	0.0387	0.258	0.0387	18.1	1.03	0.969	1.11
HD314	314-1d	3.92	8.78	1.00	4.30	0.974	0.223	1.01	0.133	0.814	0.133	0.400	0.0478	0.336	0.0458	22.1	1.02	0.958	1.06

$Ce/Ce^* = 2Ce_N/(La+Pr)_N$; $Pr/Pr^* = 2Pr_N/(Ce+Nd)_N$.

[a]The ratio of PAAS-normalized Nd and Yb.

Figure 1

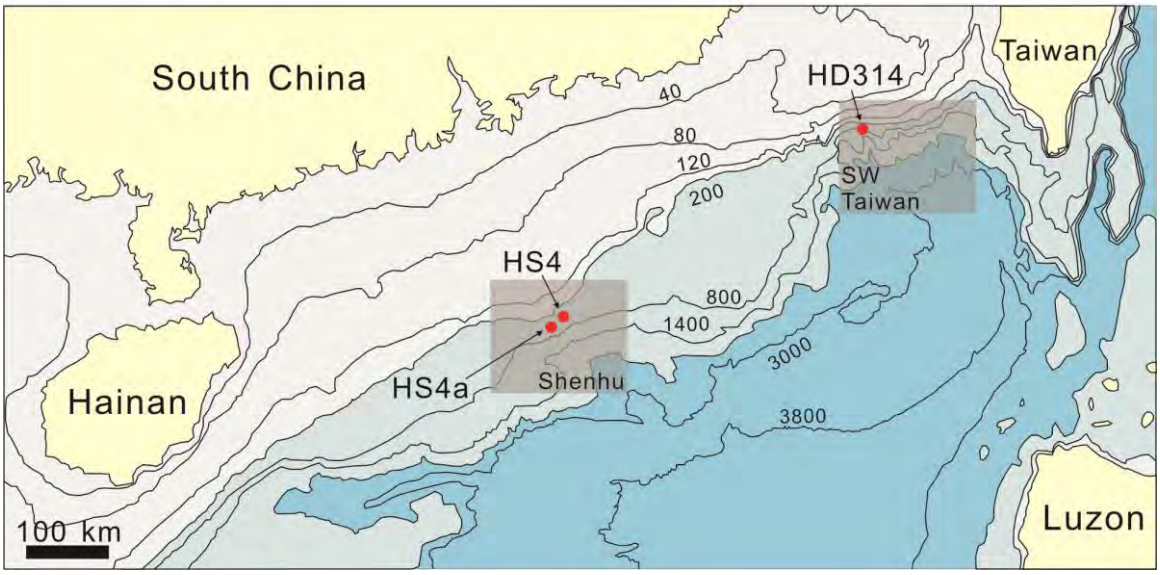

998

999

1000

Figure 2

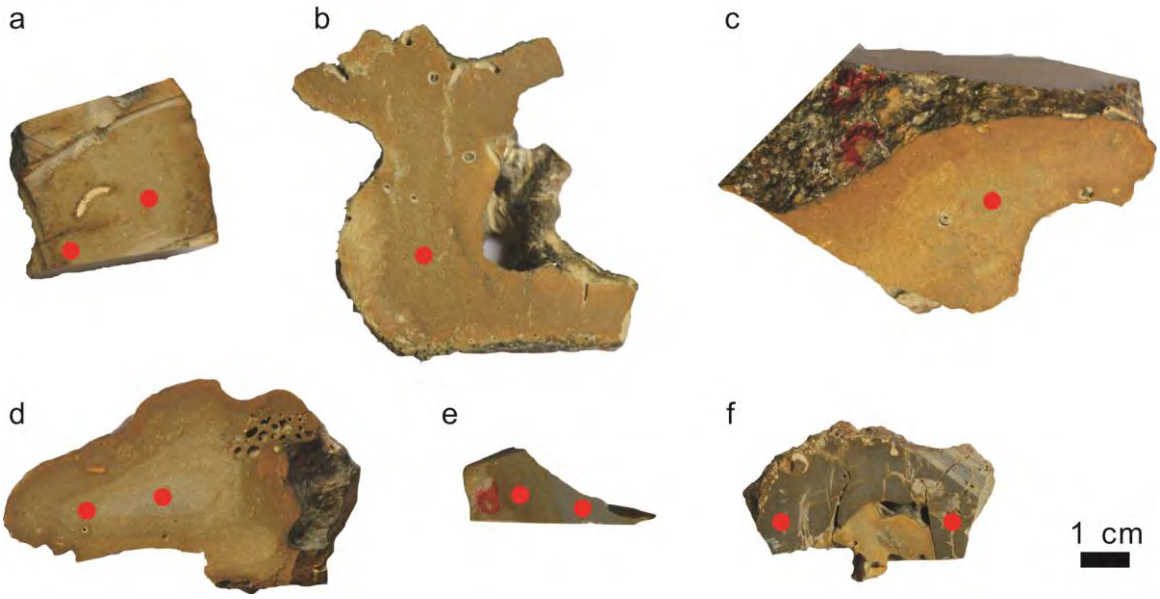

1001

1002

Figure 3

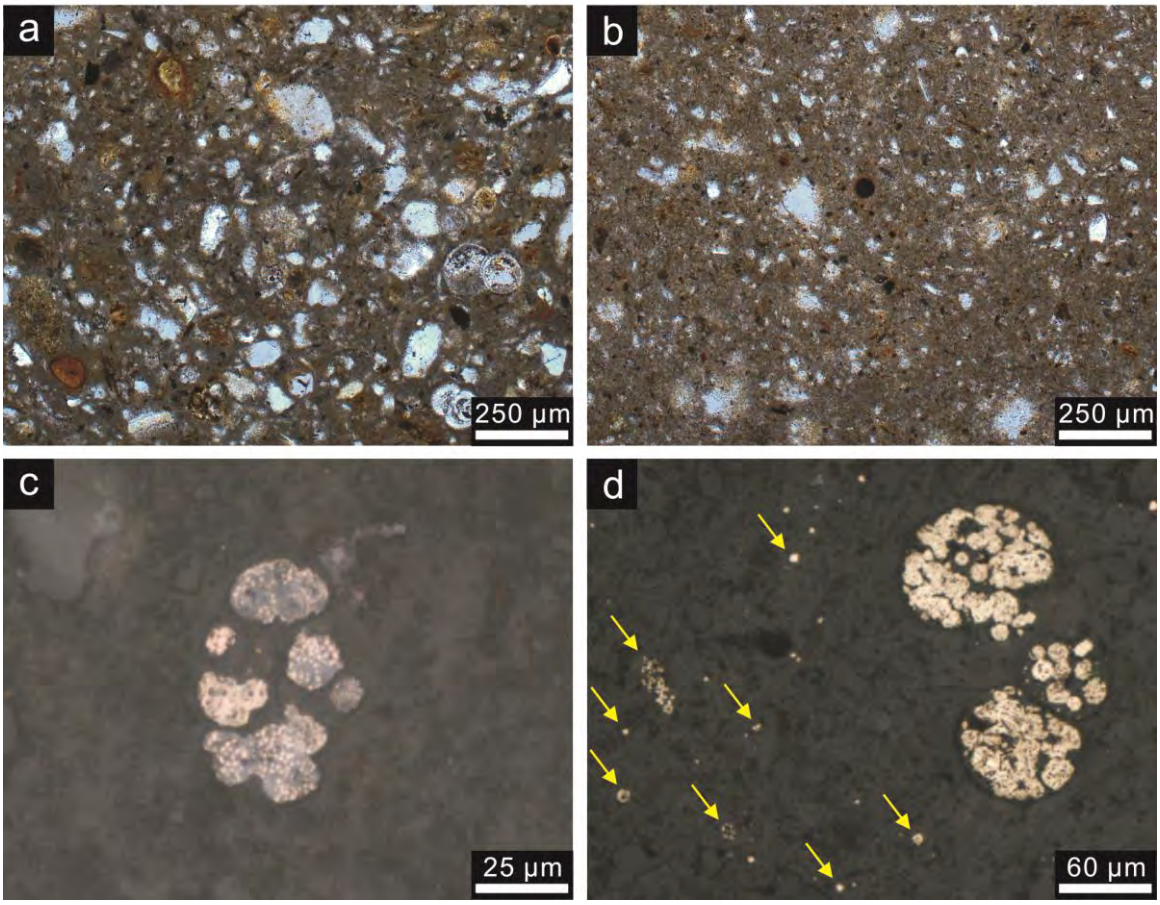

1003

1004

Figure 4

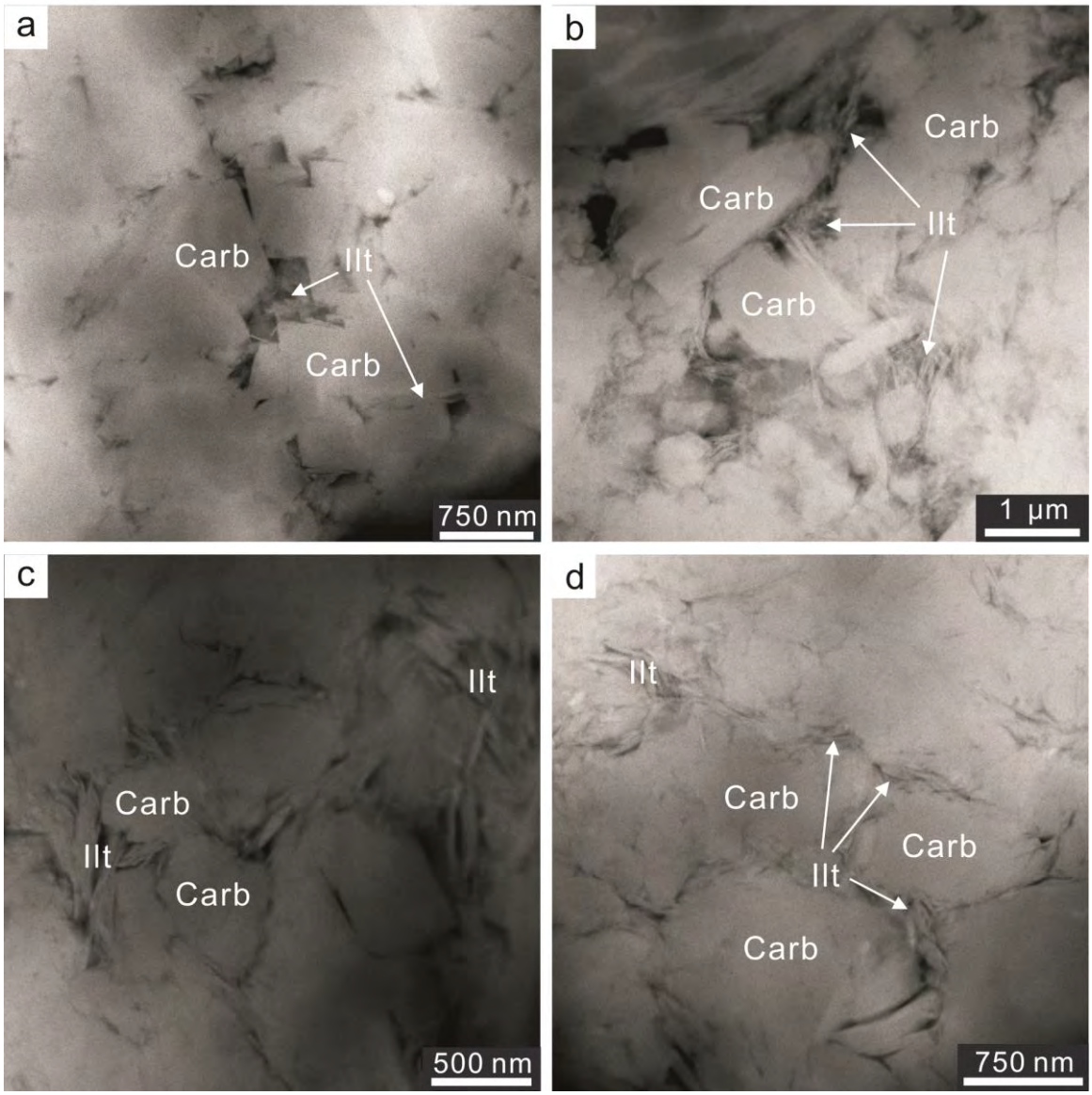

1005

1006

Figure 5

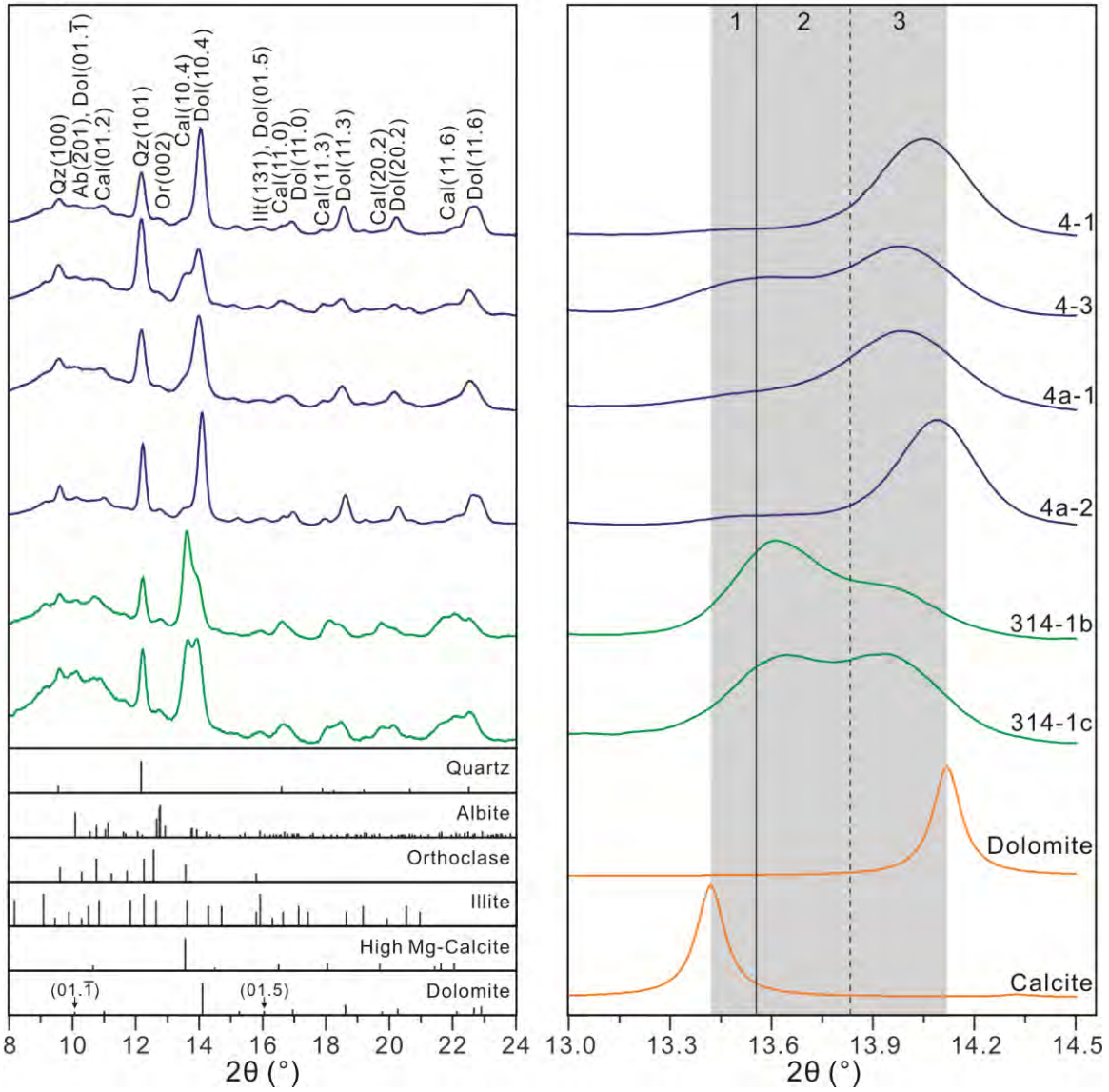

1007

1008

Figure 6

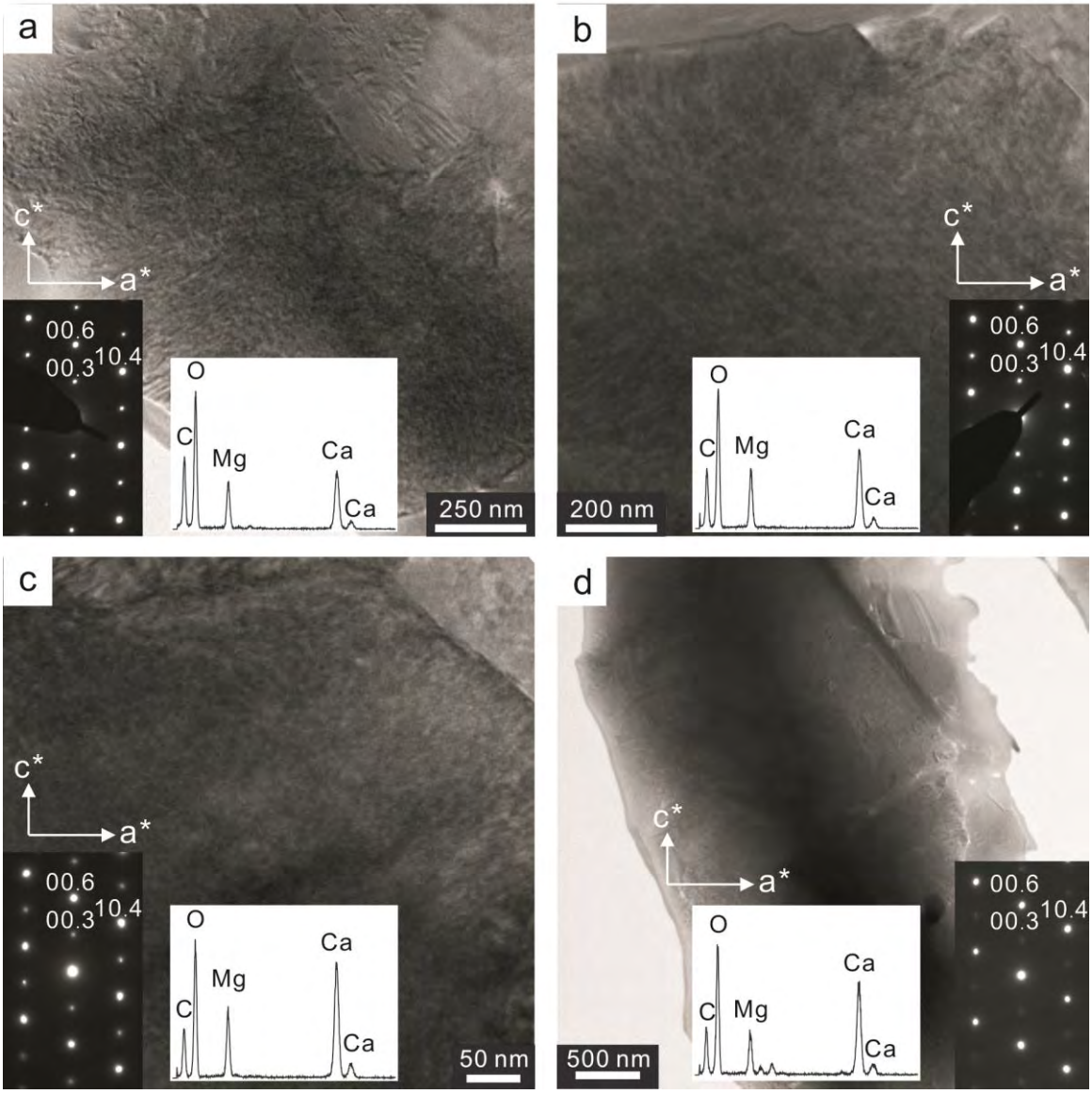

1009

1010

Figure 7

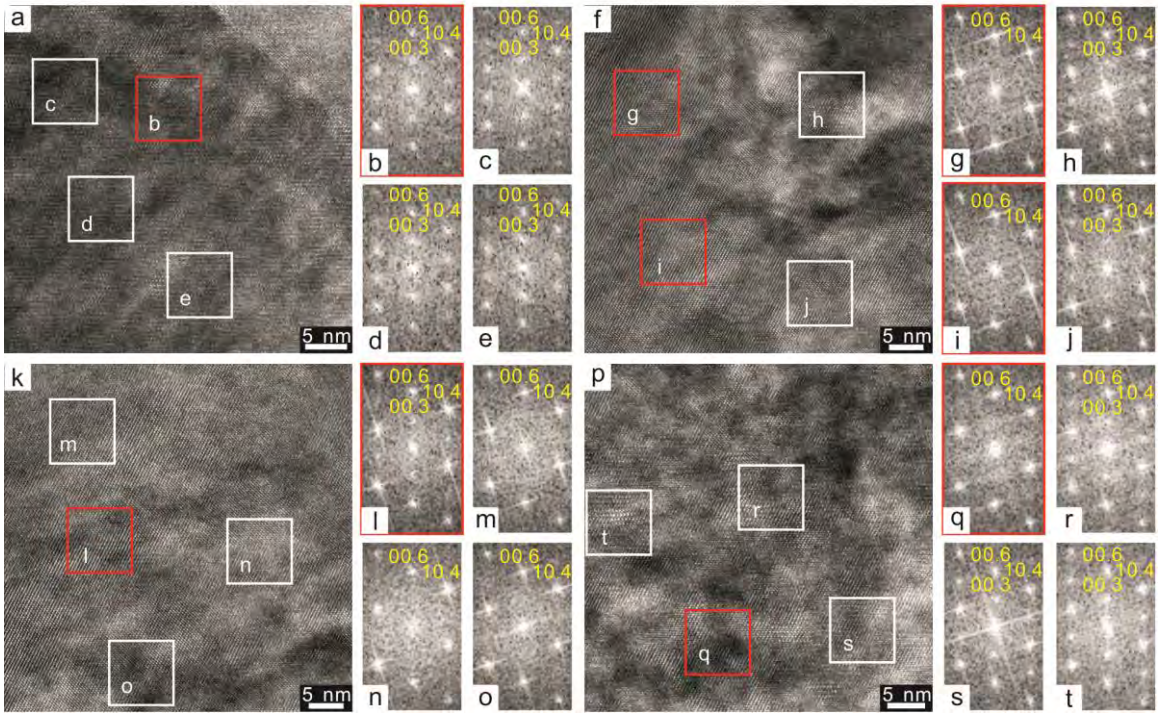

1011

1012

Figure 8

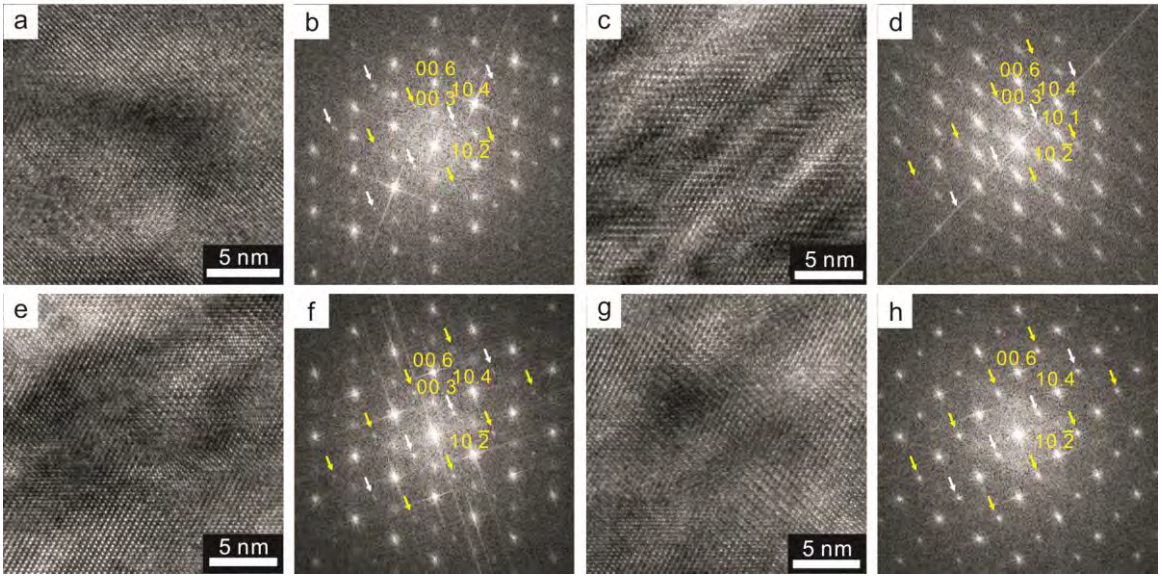

1013

1014

Figure 9

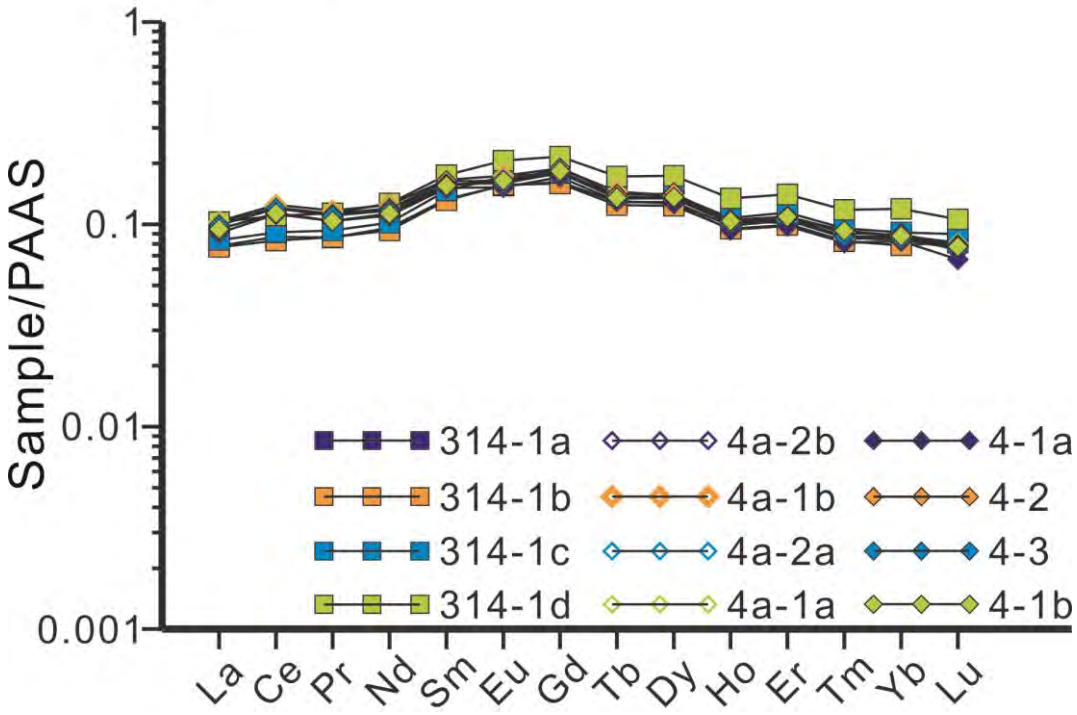

1015

1016

Figure 10

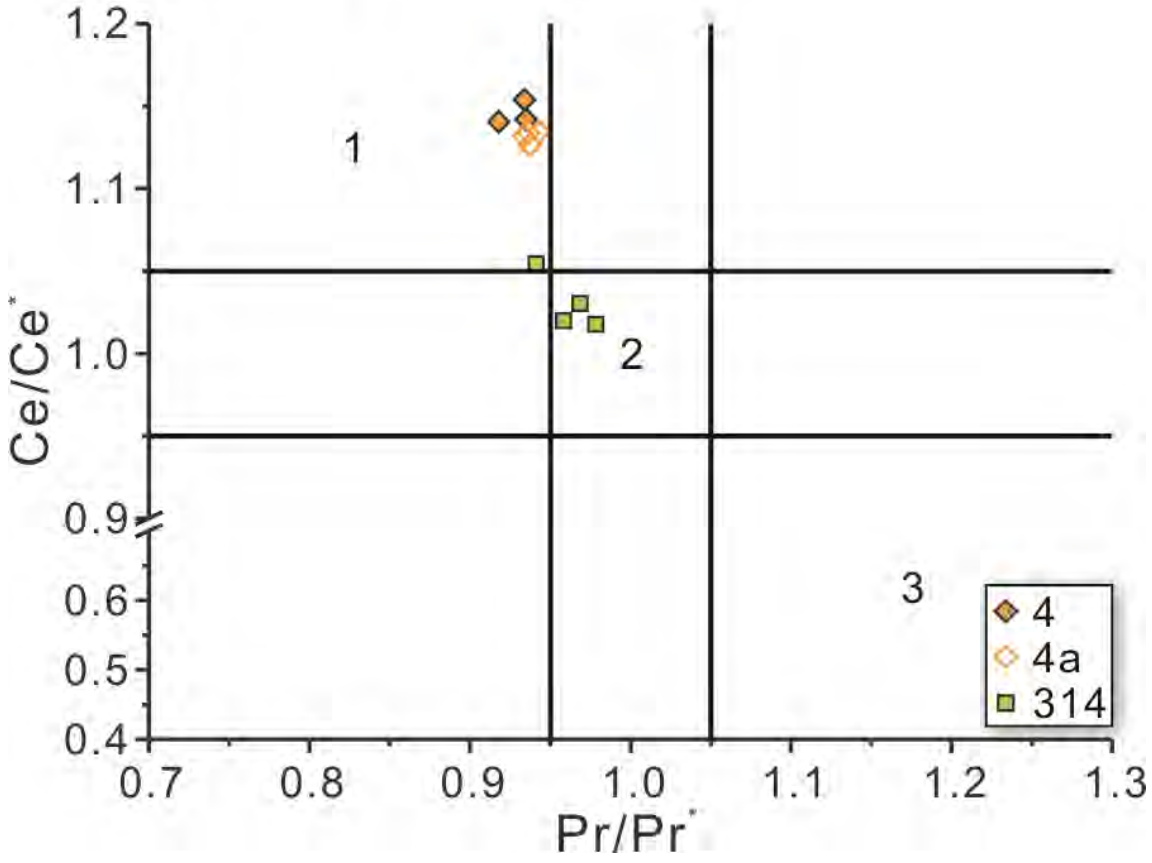

1017

1018

Figure 11

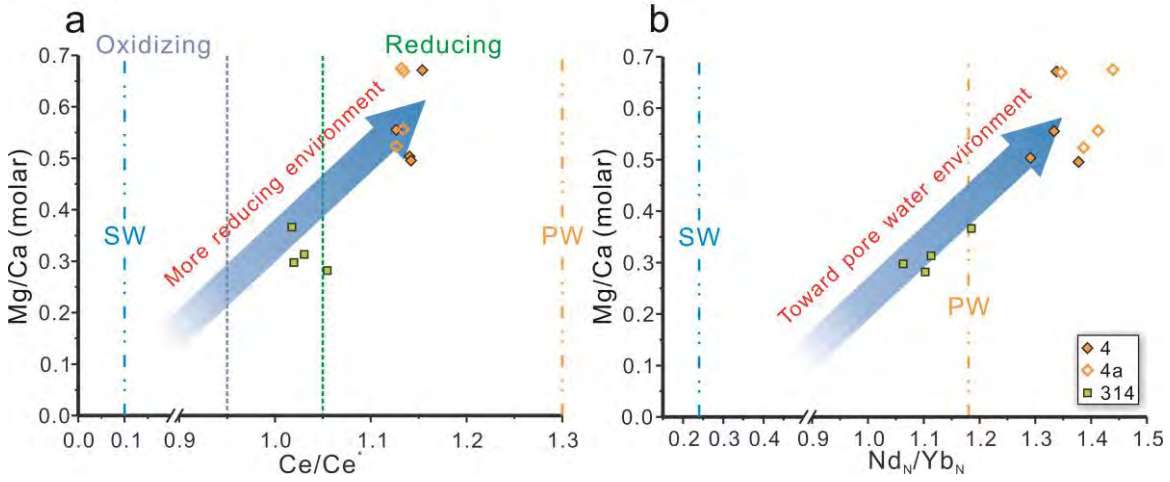

1019

1020

Figure 12

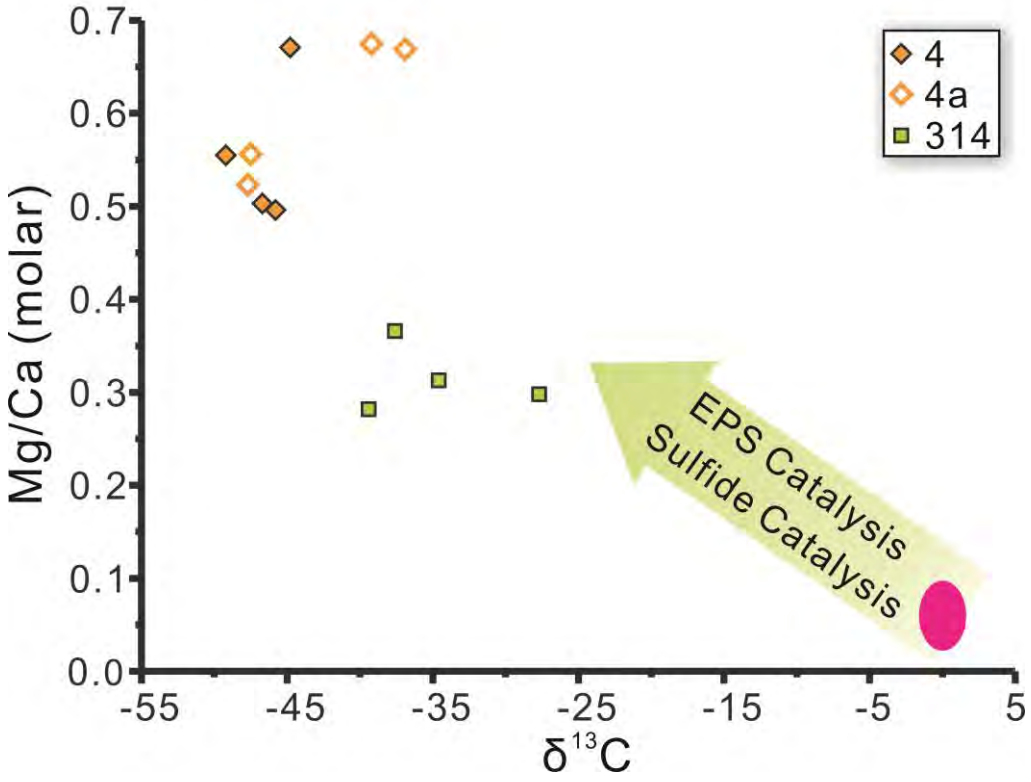

1021

1022

Figure 13

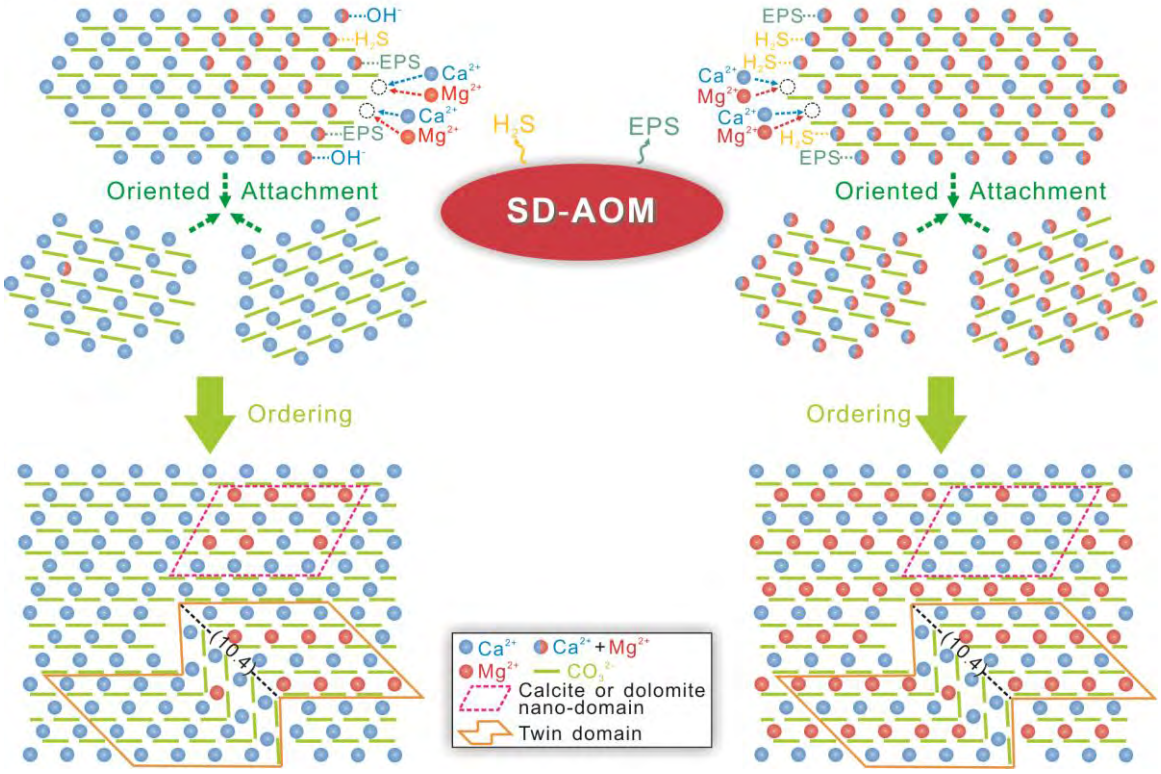

1023

1024